Green and Regioselective Approach for the Synthesis of 3-Substituted Indole Based 1,2-Dihydropyridine and Azaxanthone Derivatives as a Potential Lead for SARS-CoV-2 and Delta Plus Mutant Virus: DFT and Docking Studies

Kamalraja Jayabal,* Dhanasekar Elumalai, Saraswathi Leelakrishnan, Suman Bhattacharya, Venkatesan Rengarajan, Tharanikkarasu Kannan, and Shih-Ching Chuang*
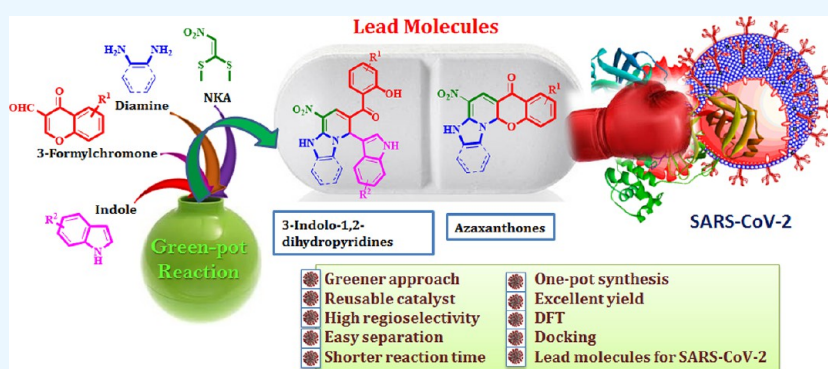
Read Online

ACCESS | Metrics & More | Article Recommendations | Supporting Information

ABSTRACT: Great attempts have been done for the development of novel antiviral compounds against SAR-CoV-2 to end this pandemic situation and save human society. Herewith, we have synthesized 3-substituted indole/2-substituted pyrrole 1,2-dihydropyridine and azaxanthone scaffolds using simple, commercially available starting materials in a one-pot, green, and regioselective manner. Further, the regioselectivity of product formation was confirmed by various studies such as controlled experiments, density functional theory (DFT), Mulliken atomic charge, and electrostatic potential (ESP) surface. In addition, 3-substituted indole 1,2-dihydropyridine was successfully converted into a biologically enriched pharmacophore scaffold, *viz.*, indolylimidazopyridinylbenzofuran scaffold, in excellent yield. Moreover, the synthesized 3-substituted indole 1,2-dihydropyridine/2-substituted pyrroles were analyzed in docking studies for anti-SARS-CoV-2 properties against their main protease (M^{pro}) and anti-Delta plus properties against their protein of the Delta plus K417N mutant. Further, the drug-likeness prediction was analyzed by the Lipinski rule and other pharmacokinetic properties like absorption, distribution, metabolism, excretion, and toxicity using preADMET prediction. Interestingly, the docking results show that out of 20 synthesized compounds, 5 of them for M^{pro} of SAR-CoV-2 and 9 of them for 7NX7 spike glycoprotein's A chain of Delta plus K417N show greater binding affinity when compared with remdesivir that is the first to receive FDA approval and is currently used as a potent drug for the treatment of COVID-19. These results suggest that indole/pyrrole substituted 1,2-dihydropyridine derivatives are capable of combating SARS-CoV-2 and its Delta plus mutant.

INTRODUCTION

Severe acute respiratory syndrome coronavirus (SARS-CoV) and Middle East respiratory syndrome coronavirus (MERS-CoV) mainly cause zoonotic infections originating from the bat/civet and dromedary.[1] In 2019, a new type of coronavirus was first identified in Wuhan, a city in China, which spreads quickly by human-to-human transmission worldwide.[2] Hence, a global emergency was made on 11 Feb 2020 by the International Virus Classification Commission (ICTV) to classify the new coronavirus as "2019-nCoV". In the meantime, the World Health Organization also named the

2019-nCoV "COVID-19". The pandemic waves have been causing severe acute respiratory syndrome and other chronic illnesses to affected individuals regardless of age. Later, COVID-19 was renamed as "severe acute respiratory

Previous works

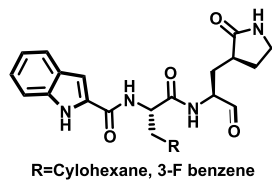**1. Indole contaning peptometrics for SARS-CoV-2 Main Protease**

R=Cylohexane, 3-F benzene

- Multi-step synthesis
- Prefunctionalized starting material
- Toxic solvent (DCM, dioxane, DMF and THF)
- Poor atom economy
- Less yield
- Tedious separation process
- $EC_{50} = 0.53 \pm 0.01 \mu M$

W. Dai *et al.*, *Science*, 2020, 368, 1331.

2. Indole moiety inhibits the Main Protease of SARS-CoV-2 and blocks virus replication

- Multi-step synthesis
- Prefunctionalized starting material
- Toxic solvent (Pyridine, DMF, CCl_4 and dioxane)
- Poor atom economy
- Less yield
- Tedious separation process
- $EC_{50} = 4.2 \pm 0.7 mM$
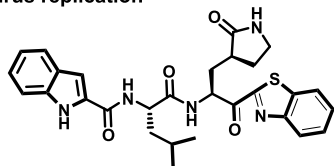
S. Hatori *et al.*, *Nat. Commun.*, 2021, 12, 668.

3. Indole based 3-chloropyridinyl ester derivative for SARS-CoV-2 3CL Protease

- 2-step synthesis
- Prefunctionalized starting
- material
- Toxic solvent (THF and DCM)
- Poor atom economy
- Less yield
- Tedious separation process
- $EC_{50} = 15 \mu M$

A. K. Ghosh *et al.*, *J. Med. Chem.*, 2021, 64, 14702.

4. Pfizer developed Indole based inhibitor for SARS-CoV-2 3CL Protease

PF-00835231

- Multi-step synthesis
- Prefunctionalized starting material
- Toxic solvent (DCM, dioxane, DMF and THF)
- Poor atom economy
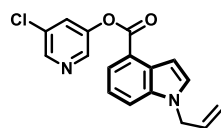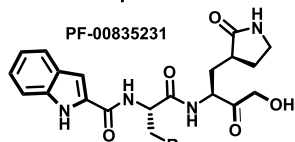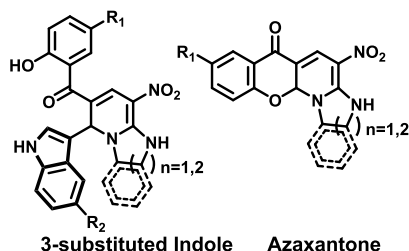- Less yield
- Tedious separation process
- $EC_{50} = 39.7 \mu M$

B. Boras *et al.*, *BioRxiv*, 2021

Our work:

- One-pot synthesis
- Single step
- Simple starting material
- Greener solvent
- High atom economy
- High yield
- Easy separation process
- Easy scalable

3-substituted Indole   **Azaxantone**

Figure 1. The recent development of indole-containing bioactive compounds for SARS-CoV-2.

syndrome coronavirus-2″ (SARS-CoV-2). An outbreak of the SARS-CoV-2 seemed inevitable due to the rapid transmission rate by infected or asymptomatic persons' aerosols and the improper social distance in affected countries .[3] Typically, symptoms of the SARS-CoV-2 include cough, fever, breathing difficulty, sore throat, diarrhea, headache, nausea, congestion, and loss of taste or smell, leading to severe respiratory problems and finally death. Therefore, SARS-CoV-2 is called a ″novel coronavirus″. The World Health Organization (WHO) statistically reports that the global pandemic distribution rate is **572,239,451** confirmed cases of COVID-19, including **6,390,401** confirmed deaths, as of 29 July 2022 in 223 countries overall. Noteworthily, the SARS-CoV-2 spike receptor protease plays a critical role in facilitating the virus invasion on the human cell receptor (angiotensin converting enzyme-2, ACE2) and the host cell receptor (transmembrane protease serine-2, TMPRSS2).[4]

Later, the pandemic rapidly moved to the second wave due to the sudden mutant of the SARS-CoV-2 spike proteins known as Delta variant B.1.617. This Delta variant seems to be around 60% more transmissible than the other variants such as Alpha (B.1.1.7), Beta (B.1.351), and Gamma (P.1) across the world; even vaccine-induced antibodies are less potent in reducing the effect of these variants because of their two E484Q and L452R mutations.[5] Very recently, the B.1.617.2 variant was identified as another new variant called Delta plus; this additional K417N mutation is expected to have a greater affinity toward lung tissues as compared to previous strains.[6] At present, no selective drugs are available for effective treatment; hence, the development of potential drugs against SARS-CoV-2 variants is essential to safeguard our society. Due to the synthetic complications of new drug discovery and their unknown mechanistic pathways against SARS-CoV-2, most research scientists and drug discovery research centers have

suggested the repurposing of some known existing potent small-molecule-based drugs such as remdesivir, hydroxychloroquine, favipiravir, pirfenidone, baricitinib camostat, and lopinavir/ritonavir based on their mechanistic actions.[7] Unfortunately, none of the above drugs could effectively cure SARS-CoV-2 except remdesivir. Regrettably, the synthesis of remdesivir involves multiple steps[8] and increased costs, and it also causes several side effects on post-COVID-19 treatment. Hence the development of superior drugs against this SARS-CoV-2 by an efficient and straightforward approach is highly desirable.

Therefore, exploring structurally diverse active drug molecules *via* multicomponent reactions (MCRs)[9] plays a vital role in drug discovery progress due to its large-scale production, fewer synthesis steps, and process efficiency for societal benefits. MCR approaches are widely used as a superior method to overcome traditional stepwise synthetic complications because of their simple operation, shorter reaction time, high atom economy, reduced toxic byproducts, easy isolation process, avoidance of the tedious column chromatography purification process, etc. Hence, MCRs have been utilized as an excellent tool for synthesizing biologically significant nitrogen-based heterocyclic compounds *via* diversity-oriented synthesis (DOS).

Nitrogen-containing heterocycles, especially indole scaffolds, exhibit various biological activities, i.e., antiviral, anti-inflammatory, anticancer, anti-HIV, antioxidant, antimicrobial, anti-tubercular, antidiabetic, antimalarial, anticholinesterase activities, etc., which makes researchers more intent on them for the development of indole-based drugs.[10] Recently, indole-based organic compounds have been identified as potential drug candidates for SARS-CoV-2, as shown in Figure 1. Specifically, in 2020, Dai *et al.* developed an indole-based antiviral drug for targeting the SARS-CoV-2 main protease.[11] In 2021, Hattori *et al.* synthesized a small molecule with an indole-benzothiazole hybrid that targets the main protease of SARS-Cov-2 and blocks viral replication.[12] Similarly, Ghosh *et al.* developed indole-chloropyridinyl derivatives that exhibited potential activity against SARS-CoV-2.[13] Recently, Pfizer developed an indole-based antiviral drug as an inhibitor of the coronavirus 3CL protease for the potential treatment of COVID-19.[14] Although these indole compounds were shown to be very much effective against SARS-CoV-2, unfortunately, they have several drawbacks such as the multiple steps, requirement of prefunctionalized starting materials, toxic solvent used, lesser yield, poor atom economy, and tedious separation process. To overcome these drawbacks, effective and green pathways are required to develop antiviral drugs for SARS-CoV-2. Recently, our research group reported a wide range of indole-chalcones using *in silico* pharmacokinetics and molecular docking studies against essential proteins of SARS-CoV-2.[15] Similarly, other classes of N-fused heterocycles such as imidazopyridine and pyridopyrimidine have shown a wide range of biological activities such as antiviral, antifungal, anticancer, anti-inflammatory, anti-ulcer, anxiolytic, antidepressant, gastrointestinal, neurotropic, stress protecting agents, etc.[16] For our drug discovery program (DDP), the existence of the potential biological profile of indole-based heterocyclic compounds, our intent is to design and develop 3-substituted indoles appended N-fused heterocycles of imidazopyridine and pyridopyrimidine *via* a one-pot MCR approach to acquire remarkable biological applications in COVID-19 disease using target-oriented synthesis (TOS).

RESULTS AND DISCUSSION

In our DDP, we utilize a nitroketene *S,S*-acetal (NKA) as an efficient synthon or versatile intermediate with multiple reactive sites to synthesize several attractive biologically active heterocyclic scaffolds *via* a simple one-pot and greener approach (see Supporting Information S2). Herein, first, we report a novel regioselective 3-substituted indole/2-substituted pyrrole based 1,2-dihydropyridine and azaxanthone scaffold using In(OTf)$_3$ as a catalyst in ethanol solvent under a reflux condition. Further, the synthesized compounds were examined against SARS-CoV-2 by docking studies. The current regioselective approach involves NKA, various nitrogen-based dinucleophiles, 3-formylchromones, and indoles in the presence of a reusable catalyst in an eco-friendly solvent under a reflux condition with a shorter reaction time, as shown in Scheme 1.

Scheme 1. Regioselective Synthesis of 3-Substituted Indole Derivatives (6)
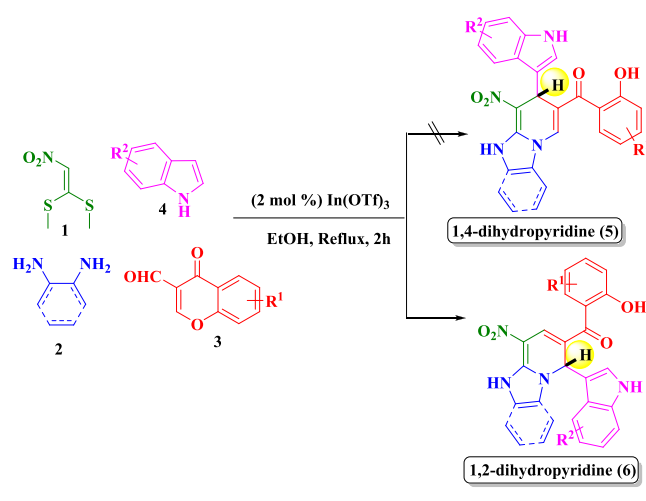
The reaction was completed within 0.5 to 2 h, and the resultant reaction mixture was purified by a simple filtration technique and gave the corresponding compounds with excellent yields. In this work, our aim was to develop biologically significant heterocycles through a novel methodology[17] and explore the chemistry of the NKA system[18] for synthesizing interesting heterocycles *via* a one-pot multicomponent reaction in a simple and eco-friendly approach.

Initially, the MCR of NKA **1**, ethylenediamine **2a**, 3-formylchromone **3a**, and indole **4a** led to the formation of 3-substituted indole **6a** that was taken as a model reaction to investigate the feasibility to optimize the reaction conditions as illustrated in Table 1. When the reaction was performed without a catalyst in ethanol as a solvent, no product formation was observed even after 24 h at ambient temperature. The same reaction was carried out in various solvent polarities such as water, methanol, acetonitrile, and toluene, including neat conditions under reflux conditions. Again, no product formation was observed even after 24 h (Table 1, entries 1 and 2). Further, the reaction was tested with an organic base, *viz.*, piperidine, and surprisingly, the product was formed at a moderate yield of 40% in ethanol used as a solvent. With the interesting result obtained from piperidine, next we tested other organic bases such as TEA, DBU, and DIPEA under the same reaction condition as well as solvent polarity, and the

Table 1. Optimization of the Reaction Conditions for 6a[a,b,c]
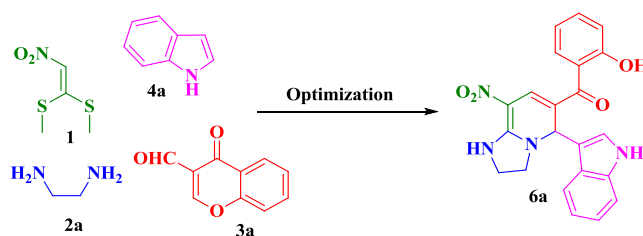
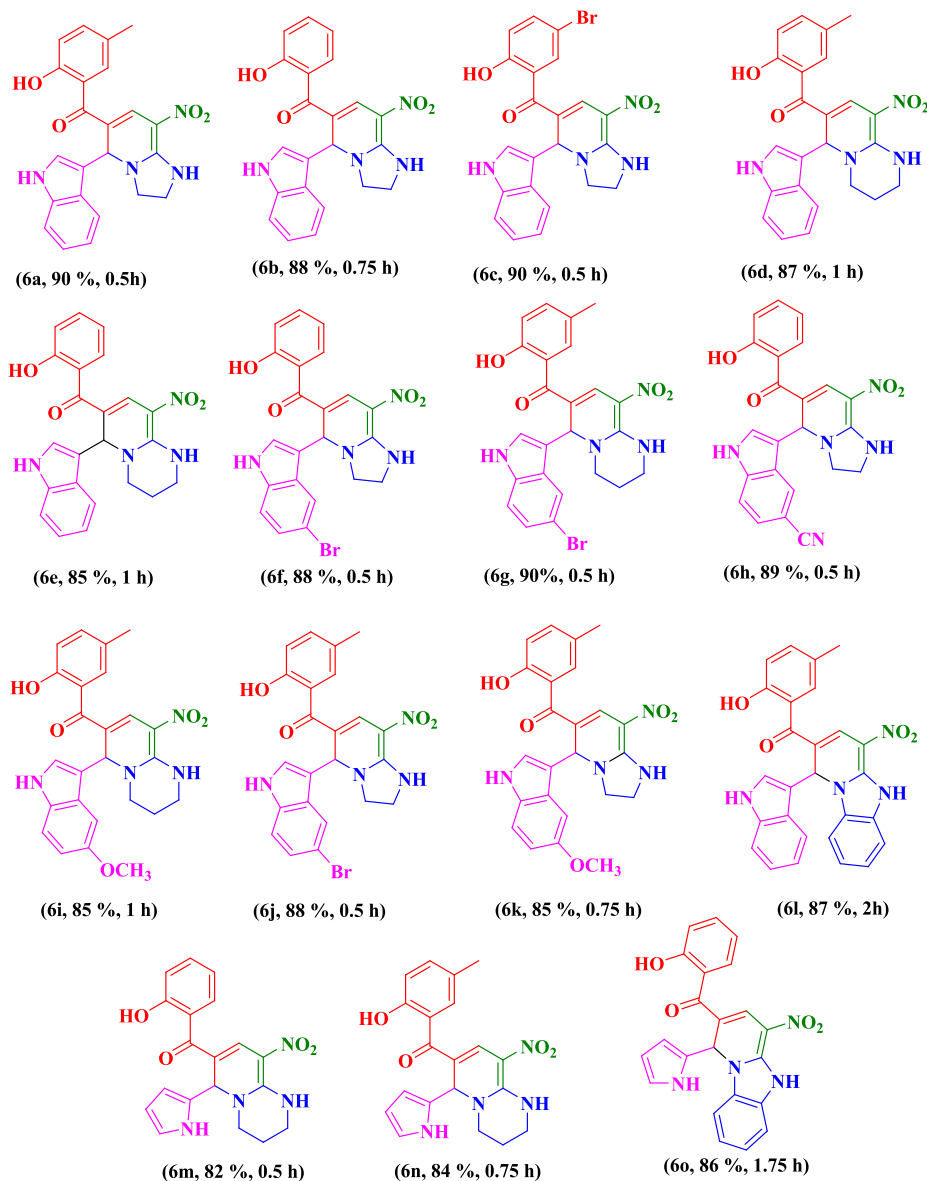|			yield (%)					
entry	catalyst (mol%)	time (h)	EtOH	water	MeOH	CH$_3$CN	toluene	neat
1	(rt)	24						
2	(reflux)	24						
3	piperidine (10)	12	40	25	35	15		10
4	Et$_3$N (10)	12	15	10	5			trace
5	DBU (10)	8	10	15	10	trace		trace
6	DIPEA (10)	8	15	20	10	5	trace	5
7	p-TSA (10)	6	35	32	25	50	15	30
8	AlCl$_3$ (10)	6	30	trace	25	37	10	15
9	InCl$_3$ (5)	2	75	65	68	58	52	40
10	In(OTf)$_3$ (5)	1	90	78	80	65	35	45
11	In(OTf)$_3$ (3)	1	90	81	84	78	61	50
12	**In(OTf)$_3$ (2)**	**0.5**	**90**	**77**	**86**	**80**	**65**	**75**
13	In(OTf)$_3$ (1)	0.5	88	74	84	78	61	72
14	Cu(OTf)$_2$ (2)	0.5	45	15	23	27	15	10
15	Cu(OTf)$_2$ (5)	0.5	48	18	25	30	15	15
16	Sc(OTf)$_3$ (5)	1	35	10	25	15	trace	10
17	Yb(OTf)$_3$ (5)	1	40	15	32	23	10	15

[a]The reaction was performed in nitroketene S,S-acetal **1a** (1.0 mmol, 0.165 g), ethylene diamine **2a** (1.0 mmol, 0.060 g), 3-formylchromone **3a** (1 mmol, 0.174 g), and indole **4a** (1.0 mmol, 0.117 g) with the catalyst (2 mol %, 0.011) in 3 mL of ethanol under reflux conditions. [b]Isolated yields. [c]Reaction time in hours.

obtained results are summarized in Table 1 (entries 3−6). To further improve the product yield, we used certain Lewis acids such as p-TSA, AlCl$_3$, InCl$_3$, In(OTf)$_3$, Cu(OTf)$_3$, Sc(OTf)$_3$, and Yb(OTf)$_3$ on the same reaction condition (Table 1, entries 7, 8, 9, 10,14, 16, and 17). Interestingly, when InCl$_3$ was used as a catalyst (5 mol %), it enhanced the reactivity with a good yield of 75% (Table 1, entry 9). Notably, when In(OTf)$_3$ was used as a catalyst (5 mol %), a notable improvement of product **6a** was observed with a 90% yield (Table 1, entry 10). Interestingly, the reaction gave a maximum yield of up to 90% when In(OTf)$_3$ 2 mol % was used (Table 1, entry 12), and further reduction of the amount of the catalyst decreased the yield (Table 1, entry13). The 2 mol % of indium triflate was sufficient to afford product **6a** in 90% yield within 0.5 h in the ethanol solvent under reflux conditions. The completion of the reaction was monitored by TLC, and the formation of product **4a** was initially confirmed by NMR spectroscopy (see Supporting Information S3). Hence, it was found as the optimized reaction condition and was used to synthesize indole substituted 1,2-dihydropyridine derivatives efficiently. Using this optimized condition, the scope of the reaction was further extended with different diamines, substituted 3-formylchromones, and indoles. To our delight, all the substituted compounds worked well and afforded diverse 3-substituted indole based 1,2-dihydropyridine derivatives **6a−l** in an excellent yield from 85 to 90% in a shorter reaction time with high regioselectivity (Table 2). For further diversity, pyrrole was used as an interesting candidate in place of indole to understand the present scope of the reaction. Interestingly, the reaction occurred very well, and the

pyrrole appended products **6m−o** were obtained in good yields (82−86%), as shown in Table 2. Based on the product formation, a plausible reaction mechanism was proposed to synthesize **6a**, as shown in Scheme 2.

In the first step, NKA **1** reacts with ethylenediamine **2** to form a cyclic N,N-acetal intermediate **A** by eliminating the MeSH. Then, the resultant intermediate **A** undergoes Henry's reaction with 3-formyl chromone **3** in the presence of In(OTf)$_3$ to form open-chain intermediate **B**. Intermediate **B** involves an intramolecular Michael addition to form a cyclic intermediate **C** with the elimination of water. Further, the **C** proceeds via a 1,3-H shift to afford azaxanthone as an interesting intermediate **7** with the assistance of the catalyst.

At this point, the regioselectivity arose due to the nucleophilic attack of indole **4** with azaxanthone intermediate **7** via two thought-provoking mechanistic pathways. Indole **4** undergoes a Michael addition reaction with azaxanthone **7** via a typical reaction path **A** to give intermediate **D** in the presence of a catalyst. Further, the intermediate **D** undergoes a chromone ring-opening reaction to give 1,4-dihydropyridine **5**, as we expected a typical Michael addition product. On the other hand, the azaxanthone intermediate **7** may undergo chromone ring-opening in the presence of a catalyst to provide pyridinium ion intermediate **F** via the reaction path **B** mechanism. The resultant pyridinium ion intermediate **F** undergoes nucleophilic attack by indole **4** to form intermediate **G**. Finally, intermediate **G** readily involves a 1,3 H-shift to give the observed product **6** with regioselectivity. In addition, there is another possibility for the formation of observed product **6** via path **C** by 1,3-isomerization of indole **4** with the expected

Table 2. Regioselective Synthesis of 3-Indolo/2-Pyrrolo1,2-Dihydropyridine Derivatives (6a−o)[a,b,c]

(6a, 90 %, 0.5h)   (6b, 88 %, 0.75 h)   (6c, 90 %, 0.5 h)   (6d, 87 %, 1 h)

(6e, 85 %, 1 h)   (6f, 88 %, 0.5 h)   (6g, 90%, 0.5 h)   (6h, 89 %, 0.5 h)

(6i, 85 %, 1 h)   (6j, 88 %, 0.5 h)   (6k, 85 %, 0.75 h)   (6l, 87 %, 2h)

(6m, 82 %, 0.5 h)   (6n, 84 %, 0.75 h)   (6o, 86 %, 1.75 h)

[a]Reaction conditions: **1** (1.0 mmol), **2** (1.0 mol), **3** (1.0 mmol), and indole/pyrrole **4** (1.0 mmol) with In(OTf)$_3$ (0.02 mmol) in ethanol (3 mL) under reflux conditions. [b]Isolated yield in %. [c]Reaction time in hours.

product **5** in the presence of the catalyst to form intermediate **E**. Further, intermediate **E** undergoes a 1,3-H shift to give product **6**.

To understand these reaction pathways and product formation, we attempted to separate all the intermediates; unfortunately, the intermediates could not be isolated except **A** and **7**, and it was revealed that intermediates **A** and **7** might be formed concomitantly and reacted instantly to give 3-substituted 1,2-dihydropyridine **6** in a straightforward approach. As shown in the proposed reaction pathway in Scheme 2, we found that the reaction goes *via* the formation of an interesting heterocycle, *viz.*, azaxanthone **7**, and acts as a key intermediate to synthesize the entire final product **6**.

Further, azaxanthone scaffolds are another class of nitrogen-based heterocyclic compounds that shows significant biological activities for the treatment of tumors and allergies and as bronchodilators.[19] Significantly, the azaxanthone-based amlexanox drug was approved by the Food and Drug Administration

(FDA) in 1996 for the treatment of aphthous ulcers and allergies and as inflammatory immunomodulators.[20] Based on the interesting biological profile of azaxanthone scaffolds, we have a plan to develop azaxanthone alone by performing a three-component reaction with the same starting materials in the absence of indole such as NKA **1**, ethylenediamine **2**, and 3-formylchromone **3** in the presence of In(OTf)$_3$ as the catalyst in an ethanol solvent under reflux conditions. After completion of the reaction, the product was separated and confirmed by NMR spectroscopy (see Supporting Information S3). To our delight, all the azaxanthone derivatives (**7a−e**) were obtained in good yields (83−87%) in the same optimized reaction condition as shown in Scheme 3 and Table 3.

Based on the fruitful results and to understand the regioselectivity of the product formation, we performed controlled experiments with compounds **6** and **4**, as shown in Scheme 4. Here, the reaction was performed with azaxanthone **7** and indole **4** using the optimized reaction

Scheme 2. A Plausible Reaction Mechanism for the Formation of Compounds 6 and 7
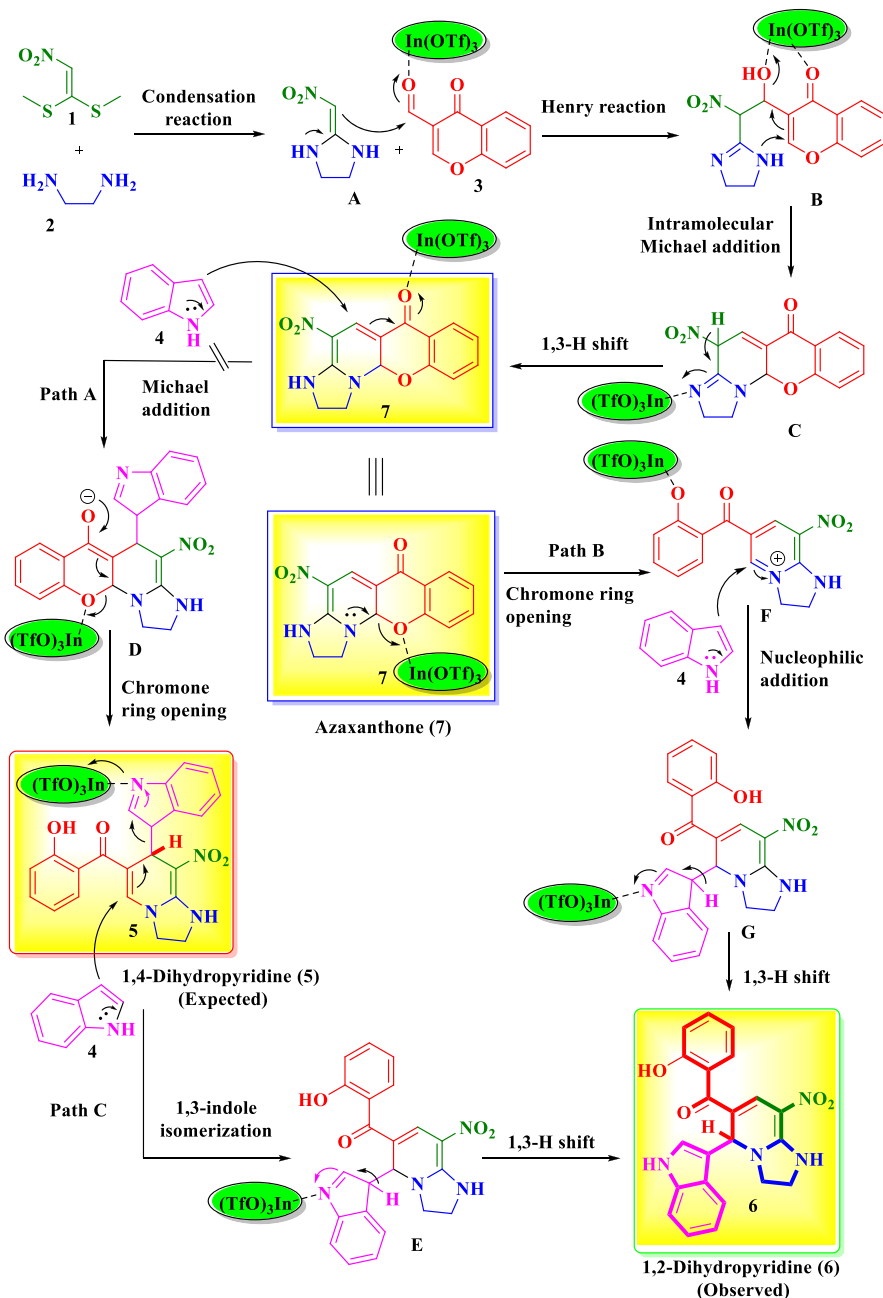

## Scheme 3. Synthesis of Azaxanthone Derivatives 7 (a−e)
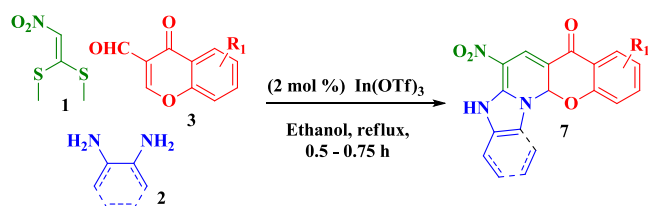
condition to get any possibility of the other regioisomer of product 5. Unfortunately, no product formation of 5 was observed as we expected, but product 6 was only formed regioselectively. Further, the same reaction was monitored by increasing the reaction time up to 12 h. Regrettably, no significant product formation of 5 and product 6 was observed

again even at room temperature. Similarly, the reaction was performed with product 6 and indole 4 under the same optimized reaction condition to get any possibility of the formation of product 5. The reaction did not proceed again, and starting materials remained unchanged. A similar fashion continued when the reaction was performed for 12 h under reflux and at room temperature individually. The observed controlled experiments strongly supported that the formation of product 6 follows only on *path* B through pyridinium ion intermediate F over the other pathways of the A or C mechanism.

To demonstrate further diversity and develop a multi-substituted dihydropyridine framework, we next performed the reaction with interesting and highly reactive heterocyclic nucleophiles such as pyrazolone, imidazole 4-hydroxycoumar-in, and 1,4-dihydroxynaphthoquinone in the place of indole

Table 3. Optimization of the Reaction Conditions for the Azaxanthone Derivatives 7 (a−e)^{a,b,c}

(7a, 87 %, 0.75 h)   (7b, 84 %, 0.5 h)   (7c, 85 %, 0.5 h)

(7d, 86 %, 0.5 h)   (7e, 83, %, 0.5 h)
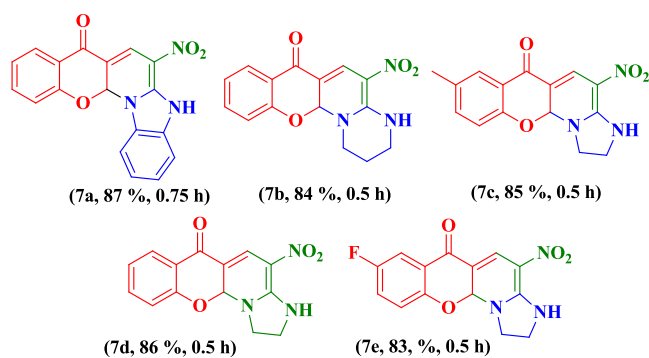
^{a}Reaction conditions: **1** (1.0 mmol), **2** (1.0 mol), and **3** (1.0 mmol) with In(OTf)$_3$ (0.02 mmol) in ethanol (3 mL) under reflux conditions. ^{b}Isolated yield in %. ^{c}Reaction time in hours.

Scheme 4. Controlled Experiments
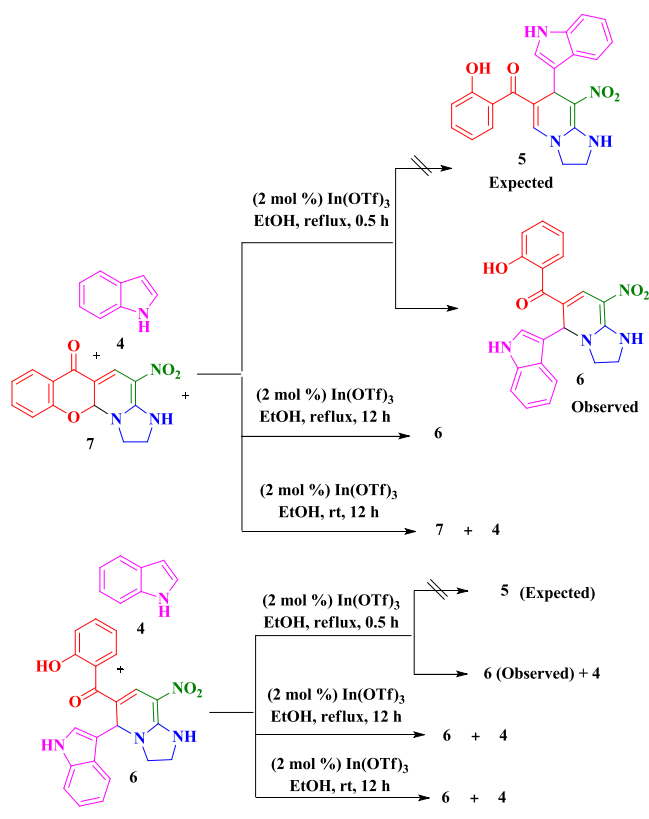
under similar optimized reaction conditions. When we used pyrazolone as a nucleophile with azaxanthone, the expected product was either pyrazole-appended 1,2-dihydropyridine or 1,4-dihydropyridine in the optimized reaction conditions. Unfortunately, the reaction did not proceed, and the starting material remained unchanged. Further, the optimized reaction condition was altered by increasing catalyst loading up to 10 mol % and reaction time up to 24 h. Unfortunately, we could not obtain any appreciable results. Similarly, the same trend was seen for all the heterocyclic nucleophiles except indole, as shown in Scheme 5.

These results reveal that the indole nucleophile reacts rapidly and selectively opens the ring of azaxanthone in a regioselective fashion compared to other nucleophiles such as

pyrazolone, imidazole, 4-hydroxycoumarin, and 1,4-dihydroxynaphthoquinone.

Moreover, the current highlight of the MCR protocol reveals that In(OTf)$_3$ acts as an interesting Lewis acid catalyst,[21] which was quickly recovered and reused in the subsequent reactions up to the sixth run (see Supporting Information S4). The catalyst yielded compound **6a** with 90% yield in the first and second runs. In the third run, we observed only a 2% loss in the yield. Even in the fourth and fifth runs, a 3% loss was observed. In the sixth run, a 5% loss was obtained. The obtained results revealed that the catalyst is highly efficient and recyclable with negligible loss in product formation. The significant highlight of the synthetic protocol is that almost all the criteria of green chemistry and sustainable principles are fulfilled. All the reactions were carried out in a less alcoholic and hazardous solvent, *viz.*, ethanol, with high atom economy with low E-factor (see Supporting Information 109) and a reusable catalyst, and mainly avoided the chromatographic separation (waste generated by separation process) for ecological concerns.

To study the scalability of the present synthetic strategy, the reaction of **1**, **2a**, **3a**, and **4a** in the presence of indium triflate was performed on a gram scale to afford the desired product **6a** in a good yield (88%, 3.664 g) after isolation as shown in Scheme 6. This easy, scalable process is beneficial in pharmaceutical industries for affordable bulk scale synthesis and commercialization of significant drug candidates.

To the best of our knowledge, this is the first example of the regioselective synthesis of 3-substituted indole and 2-substituted pyrrole-based imidazopyridine, pyridopyrimidine, and benzoimidazopyridine derivatives from nitroketene-*S*,*S*-acetal, diamines, 3-formylchromones, and indoles in the presence of In(OTf)$_3$ as a reusable catalyst in the domino one-pot reaction sequence. Remarkably, azaxanthones were also synthesized with the same starting materials without indole in optimized reaction conditions. Thus, the novel domino approach delivers a straightforward method for constructing 3-substituted indole/2- substituted pyrrole-based N-fused nitrogen heterocyclic compounds *via* a one-pot multicomponent reaction with a greener pathway.

In addition, the presence of the *o*-hydroxy ketone group at the 5-position of synthesized compounds **6a−o** makes these compounds excellent candidates as precursors for further synthetic manipulations to meet the need for diverse and useful purposes. To demonstrate the synthetic utilization of this reaction, we performed the synthetic transformations of product **6**, as highlighted in Scheme 7.

The product could be readily transformed into indolylimidazopyridinylbenzofuran derivatives (**8a−c**) through the nucleophilic substitution of substituted phenacyl bromide with the *o*-hydroxyketone group present in compound **6b** followed by an intramolecular Knoevenagel condensation reaction to obtain excellent yields (up to 93−95%) in a simple approach as shown in Table 4.

To the best of our knowledge, this is the first example of the synthesis of an indole substituted imidazole framework from *S*,*S*-acetals, diamines, 3-formylchromones, and indoles adopting interesting and unusual reaction pathways, *viz.*, condensation−Henry−intramolecular Michael addition−ring opening−nucleophilic addition−rearrangement sequence reaction, using reusable In(OTf)$_3$ as a catalyst in a simple and greener approach. Further, the synthesized indole/pyrrole substituted imidazole analogues are easily converted into

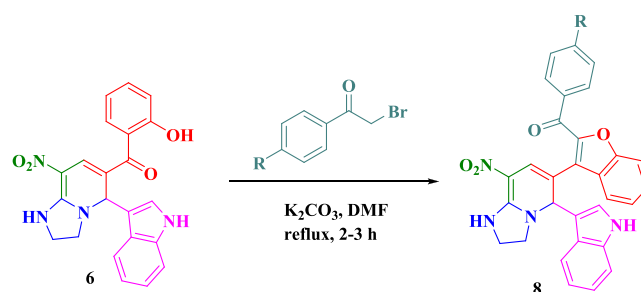**Scheme 5. Selective Ring-Opening of Azaxanthone *vs* Heterocyclic Nucleophiles**
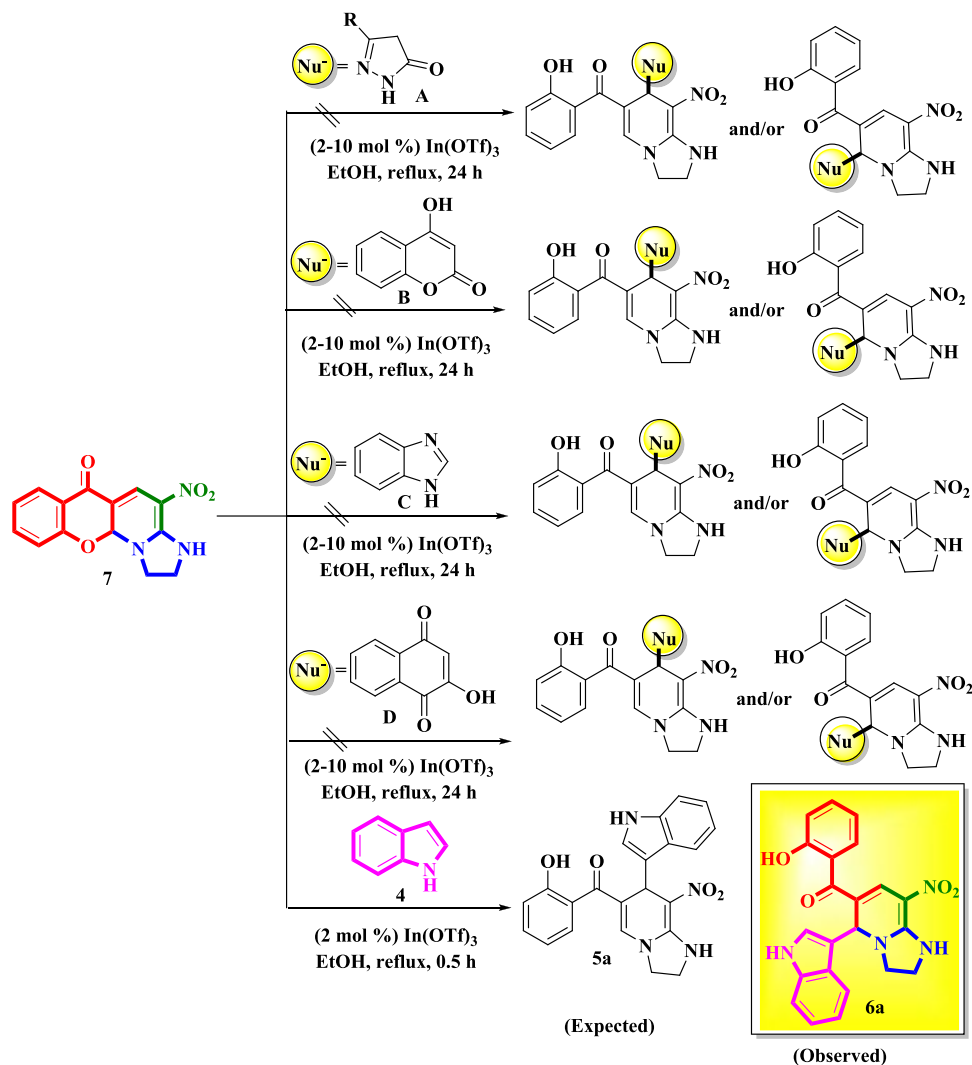
Scheme 6. Gram-Scale Synthesis of Compound 6a

Scheme 7. Synthesis of Compound 8
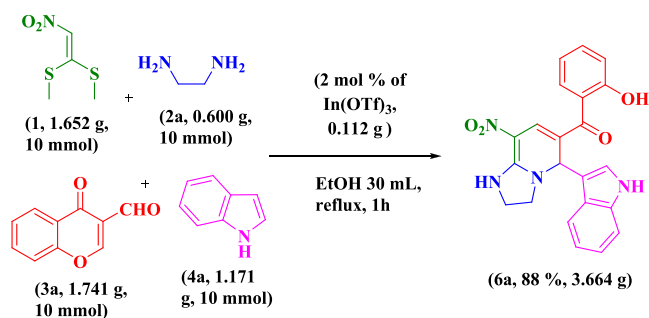
indolylimidazopyridinylbenzofuran scaffolds containing biologically significant pharmacophores, *viz.*, imidazopyridine-indole-benzofuran, with multiple functional groups in a single molecule. Further, this novel approach exhibits a very good E-factor index and high atom economy, indicating that this approach completely adopted the greener chemistry principle; hence, it is a greener approach (see Supporting Information S109).

All the synthesized compounds were characterized by various techniques such as NMR and high-resolution mass spectroscopy, and all the spectra of the synthesized compounds

were in good agreement with the proposed structures (see Supporting Information S3). Further, the synthesized **6h** compound structure was confirmed by single-crystal X-ray analysis, as shown in Figure 2 (see Supporting Information S51−S53).

Regioselectivity *via* Density Functional Theory. Further, the formation of the regioselective product of 1,2-dihydropyridine **6** has been explained through other interesting quantum chemical approaches such as Mulliken atomic charges and a map of electrostatic potential (ESP) surface for the reactive intermediate **7** as illustrated in Figure 3a,b by density functional theory (DFT) calculations using the B3LYP/6-31G
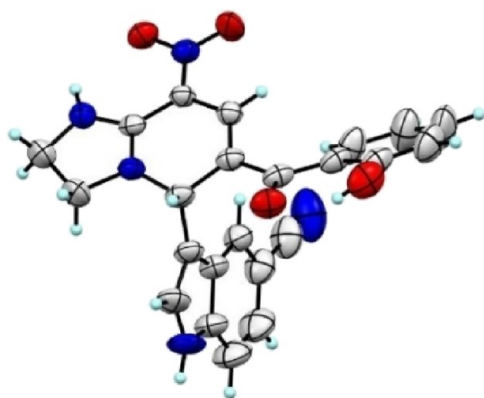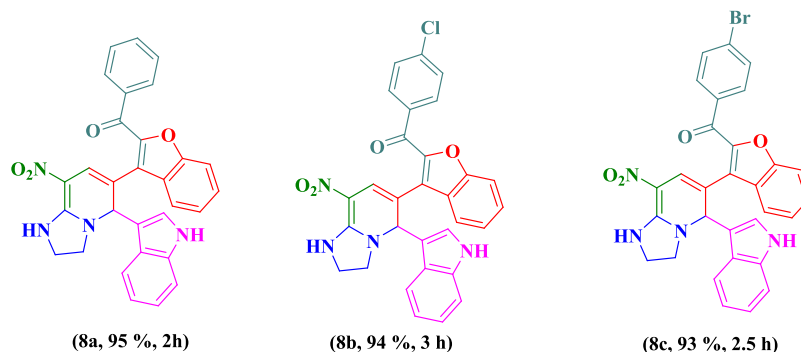
Table 4. Synthesis of Compounds 8a−c

(8a, 95 %, 2h)   (8b, 94 %, 3 h)   (8c, 93 %, 2.5 h)

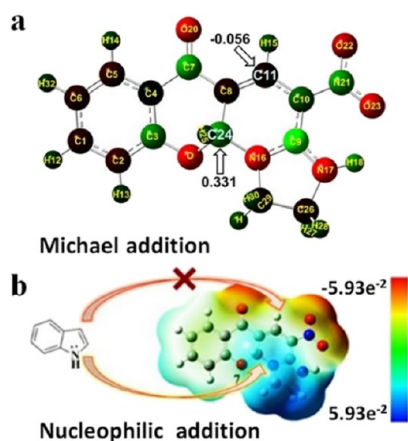**Figure 2.** Single-crystal X-ray structure of **6h** (CCDC no: 2064433).

Figure 3. (a) Mulliken atomic charge and (b) electrostatic potential (ESP) surface.

(d,p) basis set in the Gaussian 09 program.[22] According to the Mulliken atomic charge calculation of intermediate **7**, the **C-24** atom possesses a more electropositive character of 0.331 than the **C-11** atom at −0.056. This electronegativity difference leads to unfavoring of the Michael addition reaction with indole at the **C-11** atom (expected to undergo Michael addition) and favoring of the chromone ring-opening at the **C-24** atom to give **3**-substituted indole-based 1,2-dihydropyridines **6** via *path* **B** mechanism through the formation pyridinium ion intermediate **F**.

In addition, the molecular ESP surface map reveals a color scale that indicates the negative and the positive value for intermediate **7** (Figure. 3b). The red regions of a map are the most electron-rich, and the blue regions of a map are the most electron-poor regions of a molecule, as shown in Figure 3b. The azaxanthone molecule **7** has more electron-rich regions on the top due to the high electron cloud of carbonyl and nitro groups to prevent the Michael addition of incoming electron-rich indole by electrostatic repulsive force. This result favors the formation of 1,2-dihydropyridine **6** through chromone ring opening followed by nucleophilic addition *via* a *path* **B** mechanism over the Michael addition product of 1,4-dihydropyridine **5**. The observed results strongly confirm that product **6** favored the nucleophilic addition reaction over the Michael addition reaction. The presence of nitro groups at the 3-position and carbonyl groups at the 5-position on the azaxanthone moiety may drive the regioselectivity to afford the products **6**. Based on the interesting result and to explore our DDP, the efficacy of synthesized compounds, *viz.*, 3-substituted indole/2-substituted pyrrole-based 1,2-dihydropyridine and azaxanthone derivatives, was successfully investigated against SARS-CoV-2 and the Delta plus mutant *via in silico* studies. Further, the obtained results were compared to the FDA-approved antiviral remdesivir to know the structure−property relationships and the possibilities of using effective leads against COVID-19.

Structure of SARS-CoV-2. SARS-CoV-2 belongs to the spherical *β*-coronaviruses and is pleomorphic in nature.[23] The overall coronavirus structure is made up of the following structural fragments: (i) spike proteins (S), (ii) membrane proteins (M), (iii) envelope proteins (E), (iv) nucleocapsid (N), and (v) hemagglutinin-esterase dimer (HE) glycoproteins, along with RNA as the genetic material.[24] In an electron microscope, the "S" protein peripheral surface resembles a "crown" as shown in Figure 4.

The SARS-CoV-2 nucleotide analysis indicates an 80, 55, and 50% homology to SARS-CoV-1, MERS, and common cold CoV, respectively. Further, SARS-CoV-2 has a 30 kb positive-sense (single-stranded) RNA genome with 14 open reading frames (ORFs) lying under conserved gene classifications. In the conserved gene, ORF1a and ORF1ab codes located in S, M, E, and N proteins (encoded at the 3′ end) are essential for viral protein integrity. In ORF1ab, the sequences of an amino acid domain show 94.4% similarity with those of SARS-CoV.[25] The nonstructural proteins (Nsp) encoded by the pp1ab polypeptide are needed to form the replicate mechanism in Nsp1−16. Viral enzymes such as the chymotrypsin-like protease (3CL^Pro) and main protease (M^Pro) process the polypeptides to produce nonstructural proteins (Nsp1−16), which encode for endoribonuclease activity and thus play an essential role in viral replication.[26] However, 14 unique
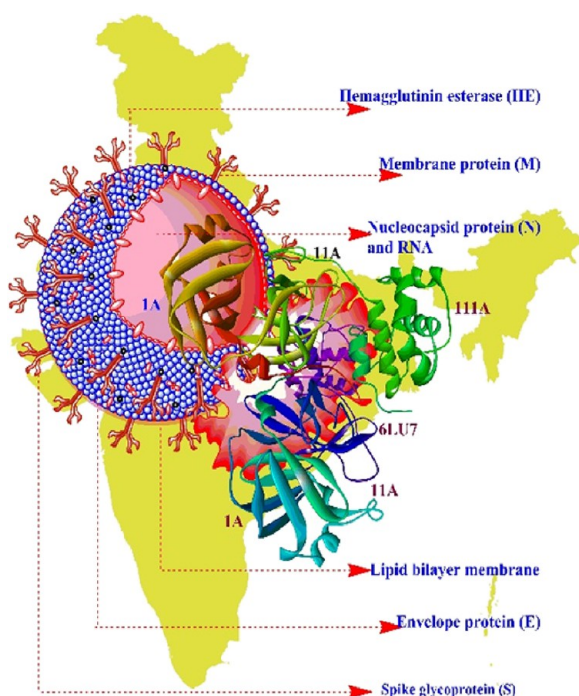
Figure 4. Structure of the SARS-CoV-2 6LU7 M[Pro].

proteolytic sites of 3CL[Pro] and papain-like protease (PL[Pro]) in SARS-CoV-2 PP1ab align with the amino acid sequence of SARS PP1ab and further restrict the cleavage sites recognized by 3CL[Pro] and PL[Pro]. The 3CL[Pro] cuts the remaining 11 sites at the C-terminus, resulting in 15 nonstructural proteins. Similarly, the PL[Pro] cleaves three sites at the N-terminus: 181−182, 818−819, and 2763−2764. The Nsp3 has several domains, including a SARS special domain section and the PL[Pro] deubiquitination and proteolytic enzyme. Likewise, the 3CL[Pro], RNA-dependent RNA-polymerase (RdRp), and helicase have Nsp5, Nsp12, and Nsp13. Thus, the protein structure biology relationship is only limited in the beginning stage of the novel coronavirus.

The SARS-CoV-2 Spike Protease Mechanistic Action against the Human Cell. A brief mechanistic action of the spike protease against humans is illustrated by the graphical representation in Figure 5. The SARS-CoV-2 spike protein cross-species transmission is facilitated by the ACE2 biomolecule, which acts as a human entry receptor. According to sequence alignment results, the spike-receptor binding domain (RBD) sequences of SARS-CoV-2 and SARS-CoV are 76% similar. Hence, SARS-CoV-2 could easily bind to the ACE2 receptor.[27] Furthermore, the spike-RBD sequence has a 95% homology between the SARS-CoV-2 and the Bat-CoV RaTG13. In the RaTG13 and the SARS-CoV-2 spike protein series, four of the five most significant amino acids (L465, L495, Y502, D510, and H514) bind to the ACE2 in the Bat-CoV RaTG13, which differ from the SARS-CoV-2. The pathogen causing the SARS-CoV-2 virus can be prevented by several pathways: (i) the target viral enzymes or functional proteins act as a blocker for virus RNA synthesis and replication; (ii) the target viral structural proteins are preventing viral entry to human cell ACE2 receptors or preventing virus self-assembly; (iii) some of the virulence factors are generated to restore the innate host immunity; and (iv) specific receptors or enzymes present in the host may prevent the virus entry into the host cells. Here, Nsp1, Nsp3

(Nsp3b, Nsp3c, PL[Pro], and Nsp3e), Nsp7 Nsp8 complex, Nsp9-Nsp10, Nsp14-Nsp16, 3CLPro, E-channel (E protein), ORF7a, spike, ACE2, helicase, RdRp, and TMPRSSS2 are the target proteins.

The papain-like protease (PL[Pro]) enzyme is responsible for the cleavage of replicate polyprotein at the N-terminus to release Nsp1, Nsp2, and Nsp3, which are needed for virus replication.[26a] The PLPro has been considered a common target for coronavirus inhibitors because of the replication enzymatic mechanism and infection of the host. For example, the antiviral drug ribavirin is expected to bind PLPro with low binding energy. Hence, the SARS-PLPro ribavirin inhibitor is bounded in the active site of the enzyme. Until now, no potential inhibitor for PLPro has been approved by the FDA for commercialization to treat the SARS-CoV-2 illness. The 3CLPro is also known as Nsp5, which cleaved automatically in the polypeptides to generate mature enzymes. Further, it cleaves the downstream of Nsps at 11 sites to release Nsp4-Nsp16.[28] The observed result revealed that the 3CLPro plays a vital role in the maturation of Nsps and is essential for the virus life cycle. The structure and enzymatic mechanism of 3CLPro have been thoroughly investigated to discover promising target drug molecules for SARS-CoV-2. Several peptide and small-molecule inhibitors are used as common inhibitors for communicable diseases like SARS-CoV 3CLPro.[29] The spike functional protein exists as a trimer on the virus surface in a unique corolla-like structure. The TMPRSS2 initiates virus invasion on the tissue. Afterward, the host cell protease TMPRSS2 cleaves spike into S1 and S2 subunits.[30] The resultant S1 subunit is found in the region (residues 14−685) of the S-N-terminal protein that contains both the receptor-binding domain (RBD) and receptor binding motif (RBM) (residues 25 and 28−32). When the S1 subunit is bound to the host cell receptor, another S2 subunit initiates the virus cell and cell membrane fusion. Both the invasion and virulence of viruses depend on the spike protein structural stability and its cleavage.[31] Hence, antiviral drugs are essential to prevent coronavirus entry via the host surface of the spike protein. All the fusion peptides (FPs), heptad repeat 1 (HR1), heptad repeat 2 (HR2), transmembrane domain (TM), and a cytoplasmic domain (CP) are located in the S2 subunit of the spike protein.[32] The spike protein binds to the ACE2 receptor, and the metastable prefusion occurs via a significant structural reorientation in the confirmation.[33] The cryo-EM analysis revealed that the ACE2 host cell binds via five hydrogen bonds with the RBD of the S-protein. The resultant ACE2-RBD complex of SARS-CoV-2 has a binding affinity of 15 nM, and it is 10 to 20 times higher than that of SARS-CoV-1.[34] Further, the entire RBD of the S-protein is recognized in the extracellular peptidase domain of ACE2 via polar residues.[35] Recently, a unique RRAR Furin cleavage boundary site between the S1 and the S2 subunits was discovered in the SARS-CoV-2, which facilitates the Furin cleavage of the S-protein of S1 and S2 subunits.[36] This cleavage was thought to be one of the main reasons for the SARS-CoV-2 being superior in cell fusion compared to SARS-CoV-1.

The neuropilin-1 (NRP1) is abundantly expressed in the respiratory and olfactory epithelium, which binds to the cleavage of the S-Furin S1 subunit. This binding may increase the viral infection in humans.[37] In addition, stimulation of the S2 subunit by the transmembrane protease serine 2 (TMPRSS2) is another contributing factor to the SARS-CoV-2 cell invasion capacity of disconnection from the S1
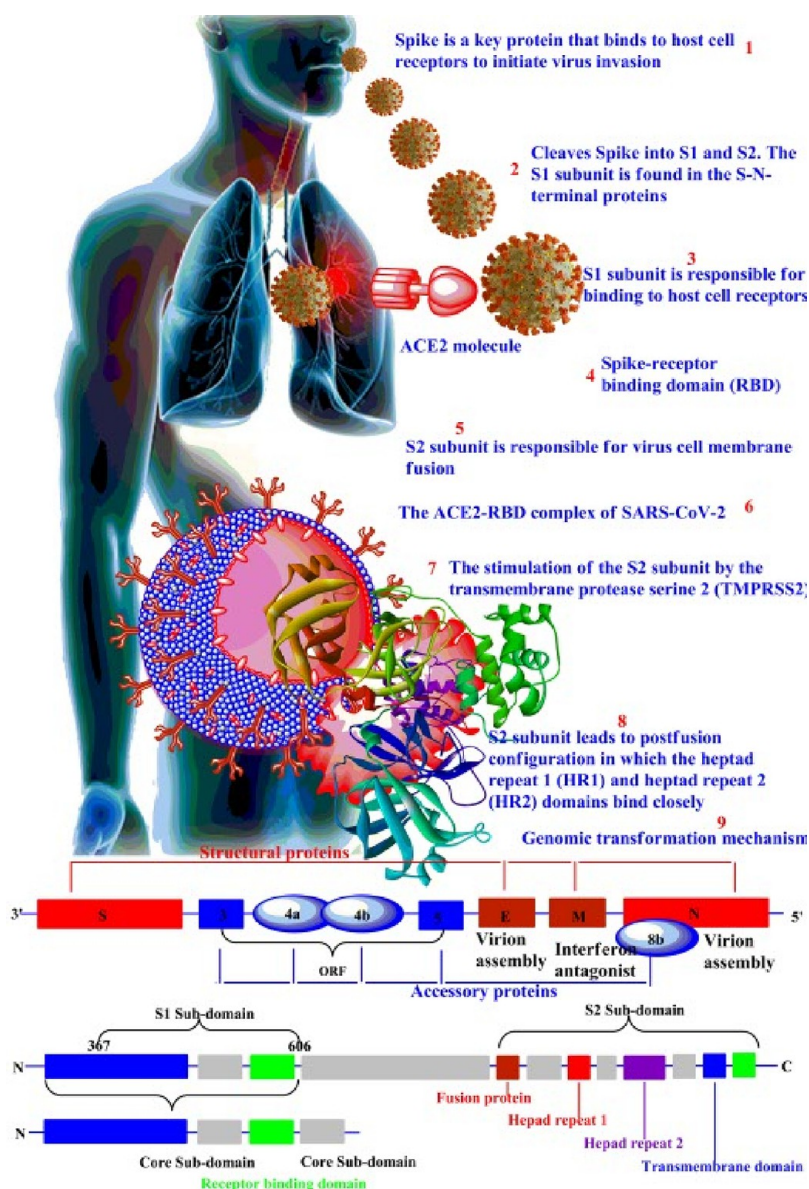
Figure 5. Graphical representation of the SARS-CoV-2 spike protease mechanism against the human cell.

subunit.[38] The priming S2 subunit leads to the reversible folding of a postfusion configuration in which the heptad repeat 1 (HR1) and the heptad repeat 2 (HR2) domains may bind closely to each other.[39] Both of these factors might have been responsible for the SARS-CoV-2 in human-to-human transmission. To suppress the interactions between the virus and host cells, ACE2 binding site antiviral drugs must be designed simply and efficiently to stop spike protein physicochemical activities. Otherwise, the furin protease, TMPRSS2 protease, NRP1, and interfaces of HR1 and HR2 domains might be critical.

6LU7 Main Protease Binding Interactions against the Synthesized 1,2-Dihydropyridines and Azaxanthones. In modern structure-based drug discovery, molecular docking is used as a powerful preliminary screenshot technique that offers a reliable way to design efficient drug molecules based on the binding affinity of noncovalent interactions of proteins (receptor) and a small molecule (drug). Herein, the SARS-CoV-2 **6LU7 M**^{Pro} crystal structure is obtained and downloaded from the RCSB Protein Data Bank (PDB).[40] At first, the

co-crystallized ligands, water molecules, and co-factors are removed before preparing protein for docking study. Now, all molecular docking calculations are demonstrated on the Auto Dock-Vina software against a series of the optimized structure (see Supporting Information S54) of all synthesized small molecules and compared with that of the FDA-approved antiviral remdesivir drug molecule to understand the structure−property relationship.[41]

To understand the **6LU7 M**^{Pro} binding interaction, we have docked with the synthesized regioselective 3-substituted indole or 2-substituted pyrrole-based 1,2-dihydropyridines and azaxanthones. Interestingly, out of 20 molecules, five of them, *viz.*, **6a**, **6c**, **6h**, **6l**, and **7a**, have shown strong binding affinity (lower docking score) compared to the FDA-approved standard drug remdesivir as shown in Table 5.

To further visualize effective binding affinity, the **6LU7 M**^{Pro} dimer, monomer, and receptor-drug binding sites (remdesivir, **6a**, **6c**, **6h**, **6l**, and **7a**) are illustrated in Figure 6. The sequential amino acid residues of the dimer are classified into three domains: IA or IA′, IIA or IIA′, and IIIA or IIIA′. This

Table 5. Compounds Show Better Docking Scores against 6LU7 Main Protein of SARS-CoV-2 Compared to Remdesivir as the Standard Drug

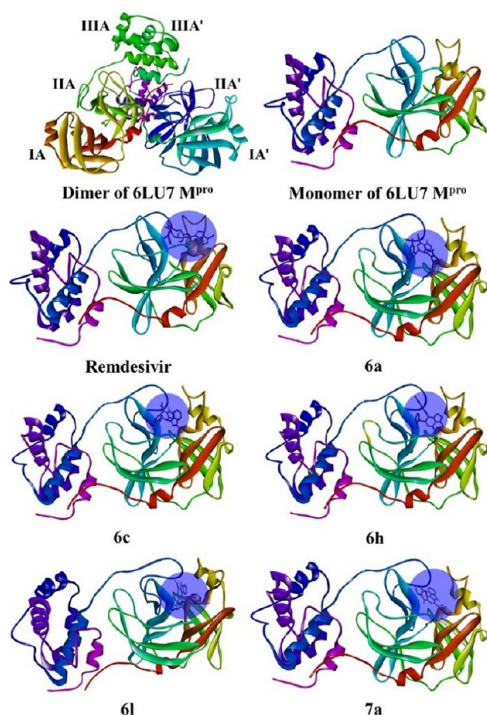| compound	protein	binding energy (kcal mol^{-1})	inhibition constant (μM)
remdesivir	6LU7 main protease	−7.7	2.269127829
6a		−8.6	0.496768633
6c		−7.8	1.916718917
6h		−8.0	1.367594556
6l		−7.9	1.619041184
7a		−8.0	1.367594556

Figure 6. Illustration of **6LU7 M^{Pro}** dimer, monomer, and receptor-drug binding site (remdesivir and lead molecules of **6a**, **6c**, **6h**, **6l**, and **7a**).

dimer is made up of two units of the A chain monomer. Interestingly, the standard antiviral remdesivir and the synthesized molecules, *viz.*, **6a**, **6c**, **6h**, **6l**, and **7a**, are strongly bounded between IA (IA′) and IIA (IIA′) domains of **6LU7 M^{Pro}** of the A chain monomer. It does clearly indicate that the synthesized compounds have exactly interacted with the specified protein fragment of **6LU7 M^{pro}** similar to the standard drug remdesivir.

Further, the developed lead molecules may strongly alter all the physiological responses *via* noncovalent interactions, *viz.*, (i) H-bonds, (ii) electrostatic interactions, (iii) hydrophobic interactions, (iv) halogen bonds, and (v) other miscellaneous interactions with that of the receptor (protein), and thereby may increase or decrease the state of protein functions. For further understanding, the hydrogen bond and noncovalent 3D receptor-side surface interactions of remdesivir, **6a**, **6c**, **6h**, **6l**, and **7a** with **6LU7 M^{Pro}** are shown in Figures 6−8 (for further details, see Supporting Information S79).

The obtained results reveal that the nature of H-bonds, other noncovalent interactions, number of interactions, molecular geometry, and a specific active site of amino acid residual interactions play a vital role in effective binding affinity
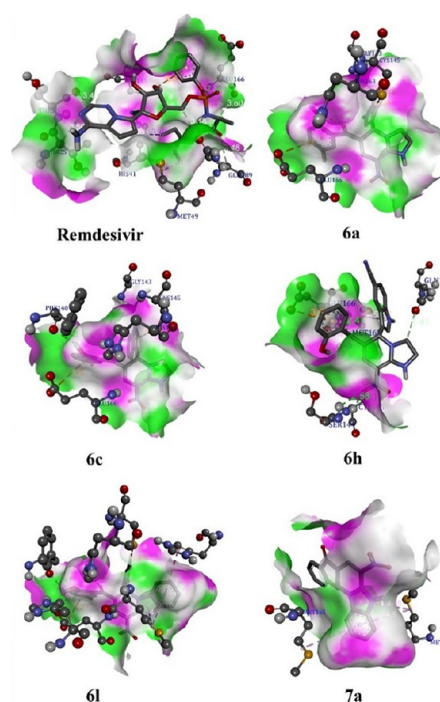

Figure 7. Map of hydrogen bond 3D receptor-side surface interaction of remdesivir and lead molecules of **6a**, **6c**, **6h**, **6l**, and **7a** against **6LU7 main protease**.

to facilitate physicochemical properties of the cellular function. Additionally, the inhibition constants for the standard antiviral drug remdesivir and the synthesized lead molecules, *viz.*, **6a**, **6c**, **6h**, **6l**, and **7a**, were calculated by using Ki = exp($\Delta G/RT$) equation, where ΔG, R, and T are the docking binding affinity, gas constant (1.9872036×10^{-3} kcal mol^{-1}), and room temperature (298.15 K), respectively. The inhibition constant (Ki) measures the overall binding affinity of lead molecules (Table 5).

At the same time, if Ki is smaller, a lesser amount of medication is needed to inhibit the cellular activity. The calculated inhibition constant (Ki) values for standard antiviral drug remdesivir and the synthesized lead molecules, *viz.*, **6a**, **6c**, **6h**, **6l**, and **7a**, are 0.496768633, 1.916718917, 1.367594556, 1.619041184, 1.367594556, and 2.269127829 μM. Here, **6a**, **6c**, **6h**, **6l**, and **7a** compounds exhibit lower Ki values than the standard antiviral drug remdesivir. Hence, these five organic molecules could have many possibilities to act as a potential lead against SARS-CoV-2. Further drug-likeness predictions are essential before practical usage.

After the severe outbreak of the COVID-19 first wave, the virus had certain specific mutations in the spike protein, *viz.*, Alpha (B.1.1.7, Kent, UK), Beta (B.1.351, South Africa), Gamma (P.1, Brazil), and Delta (B.1. 617, India). The Delta strains such as E484Q, L452R, and P614R caused an extremely deadly second wave of infections during last summer in India.

The Delta variant spikes hook onto the ACE2 receptor of the human cell, unlock, and then spread infection faster *via* replicating the virus genetic code. Unfortunately, more adults are affected by this Delta variant even though they have very strong immunity. Recently, the Delta plus of the **K417N** mutant was first identified in India and spread before completely ending the second wave. This Delta plus variant spreads more quickly and strongly and binds more to lung cells than the previous outbreaks of SARS-CoV-2 versions.
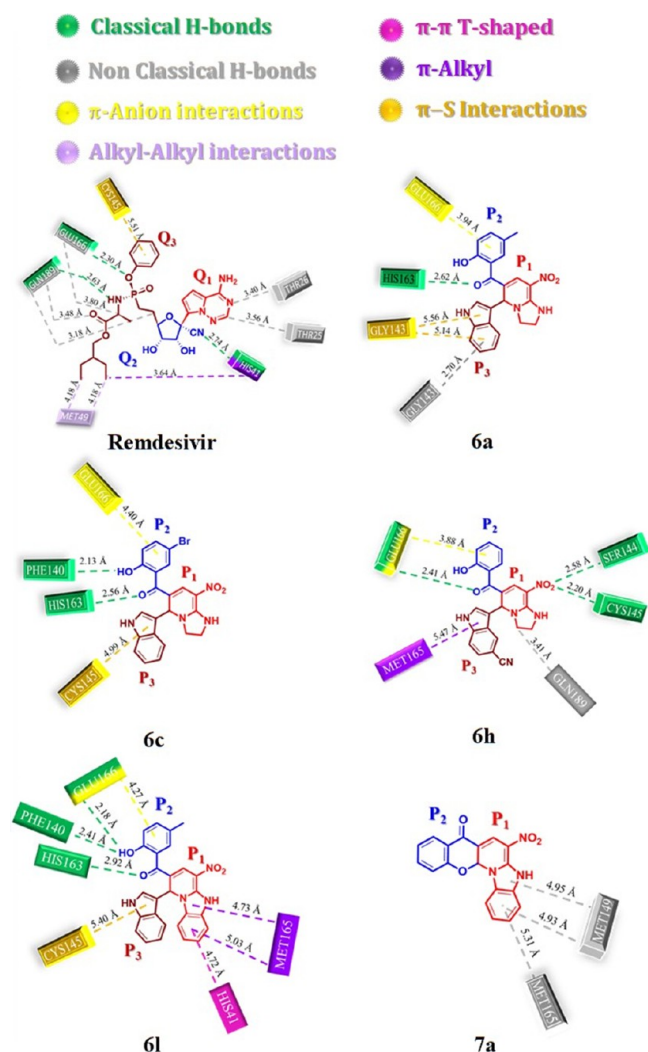
Figure 8. Schematic 2D representation of remdesivir and lead molecules of **6a**, **6c**, **6h**, **6l**, and **7a** against **6LU7** main protease.

Table 6. Compounds Show Better Docking Scores against 7NX7 Spike Glycoprotein Chain of the Delta Plus K417N Compared to Remdesivir as the Standard Drug

compound	protein	binding energy (kcal mol^{-1})	inhibition constant (μM)
remdesivir	7NX7 spike glycoprotein	−6.5	16.98940381
6a		−7.2	05.20601021
6b		−6.9	08.64272391
6c		−7.1	06.16434434
6e		−6.8	10.23369607
6h		−7.2	05.20601021
6l		−7.3	04.39666262
7a		−7.1	06.16434434
7c		−6.5	16.98940381
7e		−6.5	16.98940381
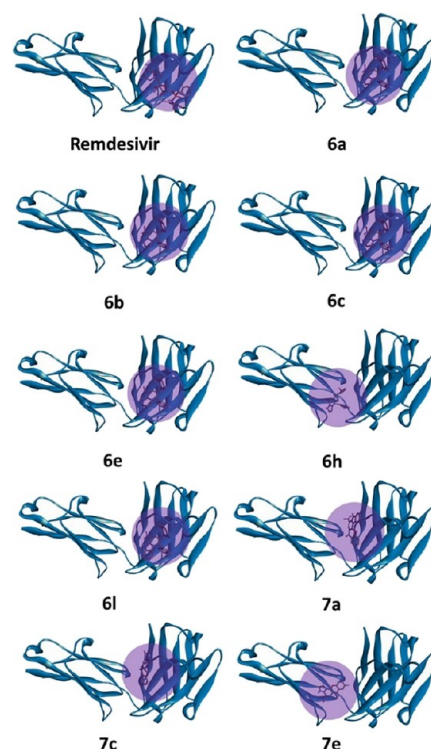
Figure 9. Photograph of K417N mutants of **7NX7** spike glycoprotein's A chain receptor-drug binding site (remdesivir and lead molecules of **6a**, **6b**, **6c**, **6e**, **6h**, **6l**, **7a**, **7c**, and **7e**).

Currently, the Delta plus variant has been found in nine countries, *viz.*, USA, UK, Portugal, Switzerland, Japan, Poland, Nepal, Russia, and China, and it is spreading worldwide. It is expected to cause a severe third wave of the pandemic. Hence, the recent outbreak of the Delta plus variant can be controlled only by the development of effective novel drugs by a simple and greener approach, which is highly desirable. Significantly, the synthesized **3**-substituted indole-based 1,2-dihydropyridines and azaxanthones showed good results against **6LU7** Main Protease of SARS-CoV-2. Next, we attempted to find the efficiency of our synthesized compounds against the **7NX7** spike glycoprotein of delta plus **K417N** mutant. The crystal structure of the **7NX7** spike glycoprotein was downloaded from the Protein Data Bank[42] (PDB code: 7NX7) and docked with all synthesized compounds.

Excitingly, out of 20 compounds, 9 compounds, *viz.*, **6a**, **6b**, **6c**, **6e**, **6h**, **6l**, **6p**, **7a**, **7c**, and **7e**, exhibit strong binding energy with a lower bind score compared to the FDA-approved standard drug remdesivir as shown in Table 6. To visualize an effective binding affinity score, the **7NX7** spike glycoprotein's A chain is selectively chosen from hetero-5-mer (chains of A, B, E, H, and L) because of the larger amino acid sequence length as shown in Figure 9 (see Supporting Information S97).

For analysis, all kinds of intermolecular interactions of 2D representation between **7NX7** spike glycoprotein and developed lead molecules (**6a**, **6b**, **6c**, **6e**, **6h**, **6l**, **7a**, **7c**, and **7e**) with the standard antiviral remdesivir drug are illustrated in Figure 8. This figure shows that our synthesized compounds were exactly interacting with the protein, which is similar to the remdesivir. In addition, the corresponding hydrogen bond 3D receptor-side surface interaction, noncovalent 3D receptor-side surface interaction, and 2D representation of the **7NX7** spike glycoprotein's A chain are shown in Figures 10 and 11 (for other compound interactions, see Supporting Information S103).

Based on the interesting results observed by *in silico* studies, 9 out of 20 of our synthesized compounds (**6a**, **6b**, **6c**, **6e**, **6h**, **6l**, **7a**, **7c**, and **7e**) are potent for the recent mutated version of the Delta plus **K417N** variant than the first outbreak version of COVID-19. Hence, it might be an effective lead molecule

Figure 10. Map of hydrogen bond 3D receptor-side surface interaction of remdesivir and lead molecules of **6a**, **6c**, **6h**, **6l**, and **7a** against 7NX7 **spike glycoprotein's A chain**.
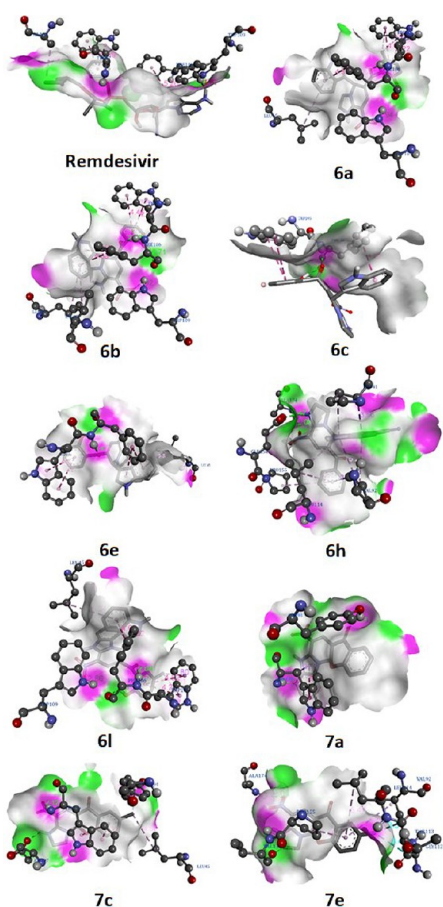
against the upcoming third wave of the Delta plus variant. Further, the drug-likeness predictions and ADMET properties were addressed to find the physicochemical properties of lead molecules to be considered effective drug candidates.

Analysis of Drug-Likeness Prediction and ADMET Properties for the Standard Antiviral Drug Remdesivir and the Synthesized Lead Molecules. The drug-likeness forecast was analyzed by the Molinspiration server with the Lipinski rule, which states that an orally active drug must comply with five laid down criteria *viz.*, molecular mass, mol LogP, hydrogen bond donor, hydrogen bond acceptor, and total polar surface area, for the synthesized nine lead compounds as shown in Table 7.[43]

In addition, over 90% of a drug can be absorbed if the TPSA value is <60 Å^2. It is a significant hydrogen bonding correlation of a molecule for the bioavailability of a drug molecule. The obtained results suggest that all the developed lead compounds **6a**, **6b**, **6c**, **6e**, **6l**, **6h**, **6p**, **7a**, **7c**, and **7e** did not violate Lipinski's rule. Unfortunately, the standard antiviral drug remdesivir violated Lipinski's rule; *viz.*, it had more hydrogen bond acceptors (14) and higher TSPA (203.57 Å^2). Similarly, other drug-likeness rules such as CMC (Comprehensive Medicinal Chemistry), WDI (World Drug Index), and MDDR (Modern Drug Data Report) were measured using the preADMET server,[44] as shown in Table S8 (see Supporting information S106).

If the developed lead molecules are found to be suitable and qualified and to have a drug-like/mild structure and 90% cutoff
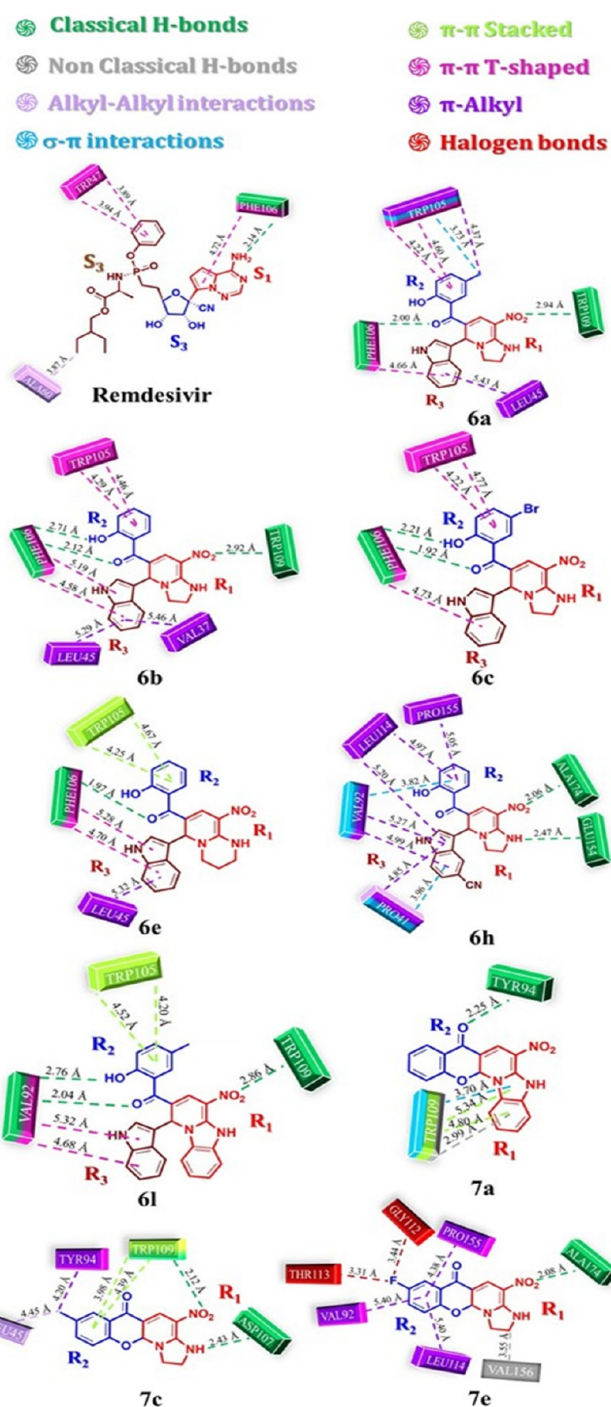
Figure 11. Schematic 2D representation of remdesivir and lead molecules of **6a**, **6b**, **6c**, **6e**, **6h**, **6l**, **7a**, **7c**, and **7e** against 7NX7 **spike glycoprotein's A chain**.

value, they should be considered potential lead molecules for real applications. The obtained results suggest that the predominant synthesized compound has a better chance of being used as a potential lead for all SARS-CoV-2.

The ADMET properties, including absorption, distribution, metabolism, excretion, and toxicity, are predicted using the preADMET server for evaluating drug selection, as shown in Table 8. The obtained database of the (i) blood−brain barrier (BBB) penetration, (ii) plasma protein binding (PPB), (iii) MDCK, (iv) human intestinal absorption (HIA), and (v)

Table 7. Drug-Likeness Prediction Analysis by the Lipinski Rule for Remdesivir, 6a, 6b, 6c, 6e, 6h, 6l, 6p, 7a, 7c, and 7e

compound	molecular weight	mol LogP	hydrogen bond donor	hydrogen bond acceptor	TPSA (A^2)
			Lipinski's rule		
remdesivir	602.59	2.82	5	14	203.57
6a	416.44	2.68	3	8	114.18
6b	402.41	2.26	3	8	114.18
6c	481.31	3.04	3	8	114.18
6e	416.44	2.88	3	8	114.18
6h	455.47	3.03	3	9	137.97
6l	464.48	5.25	3	8	119.64
7a	333.30	3.00	1	7	92.85
7c	299.29	0.86	1	7	87.39
7e	303.25	0.57	1	7	87.39

Table 8. Drug-Likeness Prediction Analysis by PreADMET Rule for Remdesivir, 6a, 6b, 6c, 6e, 6h, 6l, 6p, 7a, 7c, and 7e

compound	BBB	PPB	MDCK	HIA	Caco-2 value
			PreADMET		
remdesivir	0.04	77.55	00.04	65.74	3.96
6a	1.24	88.58	14.13	88.87	19.63
6b	0.94	92.07	24.33	88.35	19.30
6c	1.60	94.64	00.06	91.66	17.95
6e	0.93	90.47	18.58	88.87	19.53
6h	0.11	92.15	01.42	87.10	18.58
6l	2.21	96.05	01.40	91.49	19.80
7a	1.59	100.00	16.17	96.96	05.08
7c	0.91	89.89	37.83	93.88	01.27
7e	0.76	88.07	29.18	93.04	0.52

compound	mouse	rat
	Toxicity	
	carcinogenic test	
remdesivir	positive	negative
6a	negative	positive
6b	negative	positive
6c	negative	positive
6e	negative	negative
6h	negative	negative
6l	negative	positive
7a	positive	positive
7c	negative	negative
7e	positive	negative

Caco-2 cell permeability supports the use of drug lead molecules for real-time applications.

The blood–brain barrier (BBB) is a highly selective semipermeable border of endothelial cells that prevents solutes in the circulating blood from nonselective crossing into the extracellular fluid of the central nervous system. If a compound is CNS-active, it causes unintended side effects. If a compound is inactive, it does not pass and avoids the CNS side effects. The **6a**, **6c**, **6l**, and **7a** compounds were CNS-active, and **6b**, **6e**, **6h**, **7c**, and **7e** were inactive, including the standard antiviral drug remdesivir. In plasma protein binding (PPB), the nature of the chemically weak or unbound drug (less than 90%) is highly desirable for diffusion across the cell membrane, including disposition and efficacy. The following compounds, such as **remdesivir**, **6a**, **7c**, and **7e**, exhibit less than 90% PPB

value, and these compounds were weakly bounded across the plasma protein-membrane for diffusion.

The rest of the molecules, such as **6b**, **6c**, **6e**, **6h**, **6l**, and **7a** drugs, show chemically strong bound against PPB. The percentage of human intestinal absorption (HIA) value was calculated by three main methods such as bioavailability, percentage of urinary excretion of drug material following oral administration, and the ratio of cumulative urinary excretion of drug material following oral and intravenous administration. Interestingly, the lead molecules, such as **6a**, **6b**, **6c**, **6e**, **6h**, **6l**, **7a**, **7c**, and **7e** compounds, show more than 70% of the HIA value. But unfortunately, the standard antiviral remdesivir shows a value of less than 70%, which suggests that our synthesized compounds have good absorption properties and could be easily absorbed by the human intestine. Further, the Caco-2 and MDCK cell models are also reliable for *in vitro* prediction of oral drug absorption. Notably, the synthesized compounds **6a**, **6b**, **6c**, **6e**, **6h**, **6l**, and **7a** show moderate permeability within the range of 4−70 nm s^{-1}, while **7c**, **7e** and the standard antiviral remdesivir exhibit low permeability with less than 4 nm s^{-1} in the Caco-2 cell model.

In addition, the two animal models, *viz.*, mouse and rat models, have been used in the carcinogenicity test. In the mouse model, compounds **6a**, **6b**, **6c**, **6e**, **6 h**, **6l**, and **7c** showed negative tests. In contrast, compounds **7a** and **7e** and remdesivir exhibited positive tests. Similarly, in the rat model, compounds **6e**, **6h**, **7c**, and **7e** and remdesivir exhibited negative carcinogenicity tests. Unfortunately, the rest of the five compounds, *viz.*, **6a**, **6b**, **6c**, **6l**, and **7a**, showed a positive test. Finally, the derived *in silico* and molecular docking studies concluded that the nine compounds, *viz.*, **6a**, **6b**, **6c**, **6e**, **6h**, **6l**, **7a**, **7c**, and **7e**, are expected to act as a potential anti-SARS-CoV-2 drug even for the mutant Delta plus variant.

■ CONCLUSIONS

In summary, we have developed an eco-friendly and regioselective approach for the synthesis of 3-substituted indole/2- substituted pyrrole-based 1,2-dihydropyridine and azaxanthone derivatives from nitroketene *S,S*-acetal (NKA), diamines, 3-formylchromone, and indole/pyrrole using indium triflate as a green and reusable catalyst in ethanol through a domino condensation−Henry reaction−intramolecular Michael addition−cyclization−ring opening−nucleophilic addition sequence in a one-pot multicomponent reaction. Further, the controlled experiments, selective ring-opening experiments, density function theory, Mulliken atomic charge, and electrostatic potential (ESP) surface studies strongly support the regioselectivity of the product formation of 3-substituted indole based 1,2-dihydropyridine. Moreover, the synthesized dihydropyridine was successfully converted into biologically significant motifs, *viz.*, indolylimidazopyridinylbenzofuran derivatives, in facile synthetic transformation. Further, the synthesized compounds of indole/pyrrole substituted 1,2-dihydropyridine derivatives were examined *in silico* for their pharmacokinetic properties *via* docking studies Lipinski and ADMET prediction and were confirmed as having a drug-like nature. The docking studies reveal that out of 20 compounds, 5 of them, *viz.*, **6a**, **6c**, **6h**, **6l**, and **7a**, for the main protease (M^{pro}) of SARS-CoV-2 and 9 of them, *viz.*, **6a**, **6b**, **6c**, **6e**, **6h**, **6l**, **7a**, **7c**, and **7e**, for 7NX7 spike glycoprotein's A chain of the Delta plus K417N mutant exhibit greater binding ability when compared to the antiviral drug remdesivir that is an FDA-approved drug for the treatment of COVID-19. Further, the

Lipinski rule clearly reveals that the synthesized compounds were found to be suitable and qualified and to have a drug-like/mild structure and a 90% cutoff value; they should be considered potential lead molecules. The ADMET studies reveal that data such as (i) blood−brain barrier (BBB) penetration, (ii) plasma protein binding (PPB), (iii) MDCK, (iv) human intestinal absorption (HIA), and (v) Caco-2 cell permeability support their use as effective lead molecules for real-time applications. These results clearly indicate that our synthesized compounds have the potential to suppress SARS-CoV-2 and Delta plus K417N proteins and justify their further *in vitro* and *in vivo* studies. Furthermore, this approach highlighted several benefits such as the short reaction time, reusability of the catalyst, high regioselectivity, easy separation, excellent yield, simple execution, high atom economy, eco-friendly solvents, and avoidance of chromatographic purification, and essential applications for the current COVID-19 crisis. Recently, another novel variant of SARS-CoV-2 known as the Omicron variant, B.1.1.529, was identified, and it has a larger number of mutations and caused a detrimental change in COVID-19 epidemiology. Further *in silico* studies on the Omicron variant and experimental analysis of SARS-CoV-2 variants are in progress in the microbiology laboratory.

■ GENERAL INFORMATION

Commercially available starting materials were purchased from Sigma-Aldrich and used without further purification. ^{1}H, ^{13}C{^{1}H}, and DEPT 135 NMR spectra were recorded in DMSO-d_6 using TMS as an internal standard on a Bruker Avance spectrometer at 400 and 100 MHz, respectively. Chemical shifts (δ) are given in parts per million (ppm) with reference to TMS. J values are given in hertz. The standard Bruker software was used throughout the experiment. X-ray single-crystal diffraction data were collected on X8 Kappa APEXII (Bruker). Mass spectra were recorded on HRMSESI (Q-TOF). The molecular docking Auto Dock-Vina software (v. 1.1.2) was used, which was downloaded from open source free of cost. The melting points were uncorrected. Analytical thin layer chromatography (TLC) was performed with precoated aluminum sheets of silica gel G/UV-254 of 0.2 mm thickness (Merck, Germany).

■ GRAM-SCALE SYNTHESIS OF 3-INDOLO-1,2-DIHYDROPYRIDINE 6A

A 50 mL round-bottomed flask was charged with S,S-acetal (NKA) **1** (1.652 g, 10.0 mmol), ethylene diamine **2a** (0.600 g, 10.0 mmol), 3-formylchromone **3a** (1.741 g, 10.0 mmol), and indole **4a** (1.171 mmol), and indium triflate (0.112 g, 0.2 mmol) in ethanol (30 mL) was added to the reaction mixture and heated in an oil bath at reflux conditions for 30 min. The consumption of the starting material was monitored by TLC using a simple workup. The precipitated solid was filtered and washed with two portions of ethanol (10−15 mL) and dried under a vacuum to afford the desired pure product **6a** in 88% (3.664 g) yield without further purification.

■ EXPERIMENTAL SECTION

General Procedure for the Synthesis of 3-Substituted Indole/2-Substituted Pyrrole Based 1,2-Dihydropyridine Derivatives (6a-o). A 10 mL round-bottomed flask was charged with nitroketene S,S-acetal (NKA) **1** (1.0 mmol), diamines **2** (1.0 mmol), 3-formylchromone **3** (1 mmol), and

indole/pyrrole **4** (1 mmol) in ethanol (3 mL), and indium triflate (2 mol %) was added to the reaction mixture and heated in an oil bath at reflux conditions for the stipulated period. The consumption of the starting material was monitored by TLC. The precipitated solid was filtered and washed with ethanol (2 to 3 mL) and dried under a vacuum to obtain the pure products (**6a−o**) in excellent yields (85−90%) without any further purification. The identities of all of the synthesized products were confirmed by NMR and HRMS (ESI), which were in good agreement with those of the assigned structures. The further represented compound **6h** was confirmed by single-crystal X-ray analysis.

(5-(1H-Indol-3-yl)-8-nitro-1,2,3,5-tetrahydroimidazo[1,2-a]pyridin-6-yl)(2-hydroxy-5-methylphenyl)methanone (6a). Yellow solid; yield: 90% (0.374 g); mp 205−207 °C; δ_H (400 MHz, DMSO-d_6) 11.16 (1 H, s), 9.58 (1 H, s), 9.06 (1 H, s), 7.64−7.53 (2 H, m), 7.36 (2 H, dd, J = 14.7, 5.2), 7.06 (3 H, ddd, J = 19.3, 14.8, 7.1), 6.85−6.70 (2 H, m), 6.00 (1 H, s), 3.81 (1 H, dd, J = 17.0, 9.1), 3.68−3.56 (2 H, m), 3.24 (1 H, q, J = 10.7), 2.15 (3 H, s). δ_C (101 MHz, DMSO-d_6) 192.5, 154.7, 152.7, 136.3, 133.1, 131.6, 128.9, 127.2, 126.0, 125.7, 125.3, 121.2, 120.9, 119.1, 118.4, 116.0, 112.2, 111.8, 107.8, 50.7, 46.2, 42.6, 19.8. HRMS (ESI) m/z: [M + H]$^+$ calcd for $C_{23}H_{21}N_4O_4^+$ 417.1563, found 417.1570.

(5-(1H-Indol-3-yl)-8-nitro-1,2,3,5-tetrahydroimidazo[1,2-a]pyridin-6-yl)(2-hydroxyphenyl)methanone (6b). Pale yellow solid; yield: 88% (0.354 g); mp 210−212 °C; δ_H (400 MHz, DMSO-d_6) 11.18 (1 H, s), 9.87 (1 H, s), 9.08 (1 H, s), 7.64−7.55 (2 H, m), 7.37 (2 H, dd, J = 11.3, 5.2), 7.31−7.24 (1 H, m), 7.10 (1 H, t, J = 7.2), 7.03 (2 H, t, J = 7.1), 6.89 (1 H, d, J = 8.1), 6.82 (1 H, t, J = 7.3), 6.03 (1 H, s), 3.80 (1 H, dd, J = 16.9, 9.3), 3.62 (2 H, t, J = 10.2), 3.24 (1 H, q, J = 10.7). δ_C (101 MHz, DMSO-d_6) 192.4, 155.2, 154.6, 136.3, 133.1, 131.2, 128.9, 126.0, 125.6, 125.3, 121.2, 120.9, 119.2, 118.6, 118.3, 116.2, 112.1, 111.8, 107.8, 50.8, 46.2, 42.6. HRMS (ESI) m/z: [M + H]$^+$ calcd for $C_{22}H_{19}N_4O_4^+$ 403.1406, found 403.1408.

(5-(1H-Indol-3-yl)-8-nitro-1,2,3,5-tetrahydroimidazo[1,2-a]pyridin-6-yl)(5-bromo-2-hydroxyphenyl)methanone (6c). Yellow solid; yield: 90% (0.433 g); mp 210−212 °C; δ_H (400 MHz, DMSO-d_6) 11.19 (1 H, s), 10.10 (1 H, s), 9.13 (1 H, d, J = 20.8), 7.56 (2 H, d, J = 6.4), 7.39 (3 H, ddd, J = 16.9, 8.8, 2.4), 7.10 (1 H, t, J = 7.3), 7.03 (2 H, dd, J = 13.1, 4.8), 6.84 (1 H, d, J = 8.7), 5.98 (1 H, s), 3.81 (1 H, dd, J = 17.5, 8.6), 3.69−3.55 (2 H, m), 3.23 (1 H, q, J = 10.9). δ_C (101 MHz, DMSO-d_6) 190.1, 154.6, 153.8, 136.3, 133.7, 133.2, 130.5, 129.0, 125.7, 125.3, 121.2, 120.5, 119. 2, 118.3, 112.0, 111.8, 109.6, 108.0, 50.6, 46.2, 42.6.

(6-(1H-Indol-3-yl)-9-nitro-2,3,4,6-tetrahydro-1H-pyrido-[1,2-a]pyrimidin-7-yl)(2-hydroxy-5-methylphenyl)-methanone (6d). Yellow solid; yield: 87% (0.374 g); mp 196−198 °C; δ_H (400 MHz, DMSO-d_6) 11.17 (1 H, d, J = 1.7), 10.42 (1 H, s), 9.56 (1 H, s), 7.66 (1 H, s), 7.58 (1 H, d, J = 7.9), 7.36 (2 H, dd, J = 9.5, 5.3), 7.16−6.96 (3 H, m), 6.82−6.69 (2 H, m), 5.87 (1 H, s), 3.64 (1 H, d, J = 13.0), 3.42 (1 H, dd, J = 12.0, 4.6), 3.25 (2 H, ddd, J = 25.9, 15.7, 6.4), 2.14 (3 H, s), 2.00−1.82 (1 H, m), 1.72 (1 H, dd, J = 9.0, 4.4). δ_C (101 MHz, DMSO-d_6) 192.3, 152.7, 150.3, 136.3, 132.9, 131.6, 128.8, 127.1, 125.7, 125.3, 125.1, 121.2, 121.2, 119.2, 118.6, 116.0, 112.9, 111.8, 110.0, 55.8, 45.6, 38.0, 19.8, 19.2. HRMS (ESI) m/z: [M + H]$^+$ calcd for $C_{24}H_{23}N_4O_4^+$ 431.1719, found 431.1720.

(6-(1H-Indol-3-yl)-9-nitro-2,3,4,6-tetrahydro-1H-pyrido-[1,2-a]pyrimidin-7-yl)(2-hydroxyphenyl)methanone **(6e)**. Yellow solid; yield: 85% (0.353 g); mp 201−203 °C; δ_H (400 MHz, DMSO-d_6) 11.18 (1 H, s), 10.42 (1 H, s), 9.84 (1 H, s), 7.66 (1 H, s), 7.58 (1 H, d, J = 7.9), 7.37 (2 H, d, J = 8.3), 7.26 (1 H, dd, J = 11.2, 4.2), 7.09 (1 H, t, J = 7.5), 7.02 (1 H, t, J = 7.4), 6.97 (1 H, d, J = 7.3), 6.87 (1 H, d, J = 8.2), 6.80 (1 H, t, J = 7.4), 5.88 (1 H, s), 3.64 (1 H, d, J = 13.1), 3.43 (1 H, s), 3.32−3.15 (2 H, m), 1.91 (1 H, dd, J = 8.9, 4.3), 1.72 (1 H, dd, J = 8.9, 4.3). δ_C (101 MHz, DMSO-d_6) 192.1, 155.1, 150.3, 136.3, 132.9, 131.1, 128.8, 125.8, 125.3, 125.1, 121.2, 119.2, 118.5, 116.1, 112.8, 111.8, 110.0, 55.8, 45.6, 38.0, 19.2. HRMS (ESI) m/z: [M + H]$^+$ calcd for $C_{23}H_{20}N_4O_4^+$ 416.1485, found 416.1983.

(5-(5-Bromo-1H-indol-3-yl)-8-nitro-1,2,3,5-tetrahydroimidazo[1,2-a]pyridin-6-yl)(2-hydroxyphenyl)-methanone (6f). Yellow solid; yield: 88% (0.423 g); mp 220−222 °C; δ_H (400 MHz, DMSO-d_6) 11.40 (1 H, d, J = 1.9), 9.84 (1 H, s), 9.11 (1 H, s), 7.84 (1 H, d, J = 1.2), 7.60 (1 H, s), 7.38 (2 H, dd, J = 15.5, 5.5), 7.31−7.24 (1 H, m), 7.21 (1 H, dd, J = 8.6, 1.7), 7.07−7.01 (1 H, m), 6.89 (1 H, d, J = 8.1), 6.83 (1 H, t, J = 7.4), 6.03 (1 H, s), 3.85 (1 H, dd, J = 16.6, 9.5), 3.63 (2 H, t, J = 9.7), 3.23 (1 H, q, J = 10.9). δ_C (101 MHz, DMSO-d_6) 192.2, 154.9, 154.6, 134.8, 133.3, 131.1, 128.8, 127.8, 126.7, 126.2, 123.7, 120.7, 118.6, 116.2, 113.8, 112.4, 111.9, 107.8, 50.0, 46.2, 42.6. HRMS (ESI) m/z: [M + H]$^+$ calcd for $C_{22}H_{18}BrN_4O_4^+$ 481.0511, found 481.0502.

(6-(5-Bromo-1H-indol-3-yl)-9-nitro-2,3,4,6-tetrahydro-1H-pyrido[1,2-a]pyrimidin-7-yl)(2-hydroxy-5-methylphenyl)-methanone (6g). Yellow solid; yield: 90% (0.458 g); mp 212−214 °C; δ_H (400 MHz, DMSO-d_6) 11.38 (1 H, d, J = 1.6), 10.41 (1 H, s), 9.54 (1 H, s), 7.84 (1 H, d, J = 1.2), 7.65 (1 H, s), 7.40 (1 H, d, J = 2.4), 7.35 (1 H, d, J = 8.6), 7.21 (1 H, dd, J = 8.6, 1.7), 7.06 (1 H, dd, J = 8.3, 1.6), 6.83−6.71 (2 H, m), 5.87 (1 H, s), 3.68 (1 H, d, J = 12.8), 3.43 (1 H, d, J = 10.9), 3.29−3.16 (2 H, m), 2.16 (3 H, s), 1.92 (1 H, dd, J = 9.0, 4.3), 1.77 (1 H, dd, J = 8.9, 4.3). δ_C (101 MHz, DMSO-d_6) 192.3, 152.7, 150.3, 136.3, 132.9, 131.6, 128.8, 127.1, 125.7, 125.3, 125.1, 121.2, 121.2, 119.2, 118.6, 116.0, 112.9, 111.8, 110.0, 55.8, 45.6, 38.0, 19.8, 19.2.

3-(6-(2-Hydroxybenzoyl)-8-nitro-1,2,3,5-tetrahydroimidazo[1,2-a]pyridin-5-yl)-1H-indole-5-carbonitrile (6h). Yellow solid; yield: 89% (0.380 g); mp 210−212 °C; δ_H (400 MHz, DMSO-d_6) 11.79 (1 H, s), 9.84 (1 H, s), 9.15 (1 H, s), 8.22 (1 H, s), 7.63 (1 H, s), 7.57 (2 H, d, J = 8.6), 7.47 (1 H, d, J = 8.5), 7.29 (1 H, t, J = 7.7), 7.06 (1 H, d, J = 7.1), 6.90 (1 H, d, J = 8.2), 6.84 (1 H, t, J = 7.4), 6.10 (1 H, s), 3.89 (1 H, dd, J = 17.2, 9.1), 3.73−3.58 (2 H, m), 3.22 (1 H, q, J = 10.8). δ_C (101 MHz, DMSO-d_6) 192.6, 155.3, 155.1, 138.4, 134.1, 131.6, 129.3, 128.3, 126.7, 126.4, 124.7, 124.5, 121.2, 121.1, 119.2, 116.6, 114.3, 113.6, 108.2, 101.8, 50.2, 46.7, 43.2. HRMS (ESI) m/z: [M + H]$^+$ calcd for $C_{23}H_{18}N_5O_4^+$ 428.1359, found 428.1364.

(2-Hydroxy-5-methylphenyl)(6-(5-methoxy-1H-indol-3-yl)-9-nitro-2,3,4,6-tetrahydro-1H-pyrido[1,2-a]pyrimidin-7-yl)methanone (6i). Pale yellow solid; yield: 85% (0.391 g); mp 205−207 °C; δ_H (400 MHz, DMSO-d_6) 11.00 (1 H, s), 10.41 (1 H, s), 9.55 (1 H, s), 7.67 (1 H, s), 7.33 (1 H, d, J = 2.5), 7.26 (1 H, d, J = 8.8), 7.06 (2 H, dd, J = 10.4, 1.9), 6.82−6.68 (3 H, m), 5.82 (1 H, s), 3.68 (3 H, s), 3.48−3.39 (2 H, m), 3.33−3.18 (2 H, m), 2.14 (3 H, s), 1.92 (1 H, td, J = 8.7, 4.3), 1.72 (1 H, dd, J = 8.9, 4.5). δ_C NMR (101 MHz, DMSO-d_6) δ 192.3, 153.3, 152.7, 150.5, 132.9, 131.6, 131.5, 128.9, 127.1,

125.7, 125.7, 125.4, 121.0, 116.0, 112.5, 112.4, 111.1, 110.2, 100.6, 56.0, 55.9, 54.9, 45.5, 39.8, 39.6, 39.4, 39.2, 39.0, 19.8, 18.5. HRMS (ESI) m/z: [M + H]$^+$ calcd for $C_{25}H_{25}N_4O_5^+$ 461.1825, found 461.1832.

(5-(5-Bromo-1H-indol-3-yl)-8-nitro-1,2,3,5-tetrahydroimidazo[1,2-a]pyridin-6-yl)(2-hydroxy-5-methylphenyl)methanone (6j). Yellow solid; yield: 88% (0.435 g); mp 215−217 °C; δ_H (400 MHz, DMSO-d_6) 11.39 (1 H, s), 9.58 (1 H, s), 9.09 (1 H, s), 7.83 (1 H, d, J = 1.4), 7.60 (1 H, s), 7.37 (2 H, dd, J = 15.5, 5.5), 7.21 (1 H, dd, J = 8.6, 1.7), 7.07 (1 H, dd, J = 8.3, 1.8), 6.79 (2 H, dd, J = 11.4, 4.9), 6.00 (1 H, s), 3.84 (1 H, dd, J = 17.0, 9.2), 3.63 (2 H, t, J = 9.7), 3.23 (1 H, q, J = 10.8), 2.17 (3 H, s). δ_C (101 MHz, DMSO-d_6) 192.4, 154.6, 152.6, 134.9, 133.2, 131.6, 128.9, 127.7, 127.2, 126.7, 126.0, 123.7, 120.8, 120.8, 116.0, 113.8, 112.3, 111.9, 107.7, 50.2, 46.2, 42.6, 19.8. HRMS (ESI) m/z: [M + H]$^+$ calcd for $C_{23}H_{20}BrN_4O_4^+$ 495.0668, found 495.0676.

(2-Hydroxy-5-methylphenyl)(5-(5-methoxy-1H-indol-3-yl)-8-nitro-1,2,3,5-tetrahydroimidazo[1,2-a]pyridin-6-yl)-methanone (6k). Yellow solid; yield: 85% (0.379 g); mp 209−211 °C; δ_H (400 MHz, DMSO-d_6) 11.04 (1 H, d, J = 1.7), 9.61 (1 H, s), 9.10 (1 H, s), 7.63 (1 H, s), 7.31 (2 H, dd, J = 12.8, 5.6), 7.14−7.05 (2 H, m), 6.86−6.73 (3 H, m), 5.99 (1 H, s), 3.84 (1 H, dd, J = 16.5, 9.4), 3.71 (3 H, s), 3.69−3.61 (2 H, m), 3.26 (1 H, q, J = 10.9), 2.18 (3 H, s). δ_C (101 MHz, DMSO-d_6) 192.5, 154.9, 153.4, 152.7, 133.1, 131.6, 131.4, 128.9, 127.2, 126.0, 125.9, 125.8, 120.8, 116.0, 112.4, 111.8, 111.1, 108.0, 100.4, 54.9, 50.7, 46.1, 42.6, 19.8. HRMS (ESI) m/z: [M + H]$^+$ calcd for $C_{24}H_{23}N_4O_5^+$ 447.1668, found 447.1675.

(1-(1H-Indol-3-yl)-4-nitro-1,5-dihydrobenzo[4,5]imidazo-[1,2-a]pyridin-2-yl)(2-hydroxy-5-methylphenyl)methanone (6l). Brown solid; yield: 87% (0.404 g); mp 245−247 °C; δ_H (400 MHz, DMSO-d_6) 13.54 (1 H, s), 11.21 (1 H, d, J = 2.1), 9.59 (1 H, s), 7.80−7.72 (3 H, m), 7.61 (1 H, d, J = 7.4), 7.43 (1 H, d, J = 7.9), 7.34−7.21 (4 H, m), 7.08 (1 H, dd, J = 8.3, 1.9), 7.01 (1 H, dd, J = 11.1, 4.0), 6.95 (1 H, dd, J = 11.0, 4.0), 6.77 (2 H, dd, J = 10.1, 5.0), 2.13 (3 H, s). δ_C (101 MHz, DMSO-d_6) 192.4, 152.8, 141.8, 136.2, 131.8, 131.4, 130.6, 130.2, 128.9, 127.2, 126.1, 125.8, 124.5, 124.5, 124.0, 121.1, 119.9, 119.3, 118.0, 116.1, 113.2, 112.3, 112.0, 111.9, 107.8, 51.6, 19.8. HRMS (ESI) m/z: [M + H]$^+$ calcd for $C_{27}H_{21}N_4O_4^+$ 465.1563, found 465.1533.

(2-Hydroxyphenyl)(9-nitro-6-(1H-pyrrol-2-yl)-2,3,4,6-tetrahydro-1H-pyrido[1,2-a]pyrimidin-7-yl)methanone (6m). Yellow solid; yield: 82% (0.300 g); mp 191−193 °C; δ_H (400 MHz, DMSO-d_6) 10.79 (1 H, s), 10.34 (1 H, s), 9.97 (1 H, s), 7.61 (1 H, s), 7.30 (1 H, s), 7.11 (1 H, d, J = 6.6), 6.98−6.78 (2 H, m), 6.68 (1 H, s), 5.96 (2 H, s), 5.55 (1 H, s), 3.48−3.20 (4 H, m), 1.93 (1 H, s), 1.80 (1 H, s). δ_C (101 MHz, DMSO-d_6) 192.4, 155.3, 150.6, 134.0, 131.6, 129.2, 129.1, 125.9, 120.3, 119.0, 118.6, 116.5, 110.4, 108.0, 106.7, 56.3, 46.1, 38.4, 19.4. HRMS (ESI) m/z: [M + H]$^+$ calcd for $C_{19}H_{19}N_4O_4^+$ 367.1406, found 367.1369.

(2-Hydroxy-5-methylphenyl)(9-nitro-6-(1H-pyrrol-2-yl)-2,3,4,6-tetrahydro-1H-pyrido[1,2-a]pyrimidin-7-yl)-methanone (6n). Yellow solid; yield: 84% (0.319 g); mp 187−189 °C; δ_H (400 MHz, DMSO-d_6) 10.82 (1 H, s), 10.37 (1 H, s), 9.62 (1 H, s), 7.64 (1 H, s), 7.15−7.06 (1 H, m), 6.91 (1 H, s), 6.80 (1 H, d, J = 8.3), 6.69 (1 H, s), 5.96 (2 H, dd, J = 6.1, 3.5), 5.56 (1 H, s), 3.56 (1 H, d, J = 13.2), 3.49−3.39 (2 H, m), 3.31 (1 H, d, J = 7.8), 2.21 (3 H, s), 1.95 (1 H, dd, J = 8.7,

4.4), 1.80 (1 H, dd, J = 8.7, 4.5). δ_C (101 MHz, DMSO-d_6) 192.2, 152.8, 150.4, 133.9, 131.7, 129.0, 127.3, 125.7, 120.0, 118.3, 116.1, 110.3, 110.2, 107.7, 106.5, 56.1, 45.9, 38.2, 19.9, 19.3. HRMS (ESI) m/z: [M + H]$^+$ calcd for $C_{20}H_{21}N_4O_4^+$ 381.1563, found 381.1538.

(2-Hydroxyphenyl)(4-nitro-1-(1H-pyrrol-2-yl)-1,5-dihydrobenzo[4,5]imidazo[1,2-a]pyridin-2-yl)methanone (6o). Yellow solid; yield: 86% (0.344 g); mp 201−203 °C; δ_H (400 MHz, DMSO-d_6) 13.49 (1 H, s), 11.08 (1 H, s), 9.92 (1 H, s), 8.00−7.89 (1 H, m), 7.72 (1 H, s), 7.65 (1 H, dd, J = 4.9, 1.6), 7.44−7.30 (3 H, m), 7.22−7.15 (1 H, m), 7.02−6.86 (3 H, m), 6.66−6.58 (1 H, m), 6.13 (1 H, s), 5.87 (1 H, dd, J = 5.5, 2.6). δ_C (101 MHz, DMSO-d_6) 192.2, 155.2, 141.6, 132.3, 131.5, 130.7, 130.2, 129.2, 128.8, 126.0, 124.6, 124.2, 119.0, 118.8, 118.3, 116.4, 113.3, 112.0, 108.0, 107.8, 107.6, 51.0. HRMS (ESI) m/z: [M + H]$^+$ calcd for $C_{22}H_{17}N_4O_4^+$ 401.1250, found 401.1239.

General Procedure for the Synthesis of Azaxanthone derivatives (7a−e). A 10 mL round-bottomed flask was charged with nitroketene S,S-acetal (NKA) **1** (1.0 mmol), diamines **2** (1.0 mmol), and 3-formylchromone **3** (1 mmol) in ethanol (3 mL), and indium triflate (2 mol %) was added to the reaction mixture and heated in an oil bath at reflux conditions for the stipulated period. The consumption of the starting material was monitored by TLC. The precipitated solid was filtered and washed with ethanol (2 to 3 mL) and dried under a vacuum to obtain the pure products (**7a−e**) in excellent yields (83−87%) without any further purification. The identities of all of the synthesized products were confirmed by NMR and HRMS (ESI), which were in good agreement with those of the assigned structures.

6-Nitro-5H-benzo[4,5]imidazo[1,2-a]chromeno[3,2-e]-pyridin-8(13aH)-one (7a). Yellow solid; yield: 87% (0.289 g); mp 240−242 °C; δ_H (400 MHz, DMSO-d_6) 13.76 (1 H, s), 8.02 (1 H, s), 7.95−7.85 (2 H, m), 7.76 (1 H, dd, J = 6.1, 2.8), 7.72−7.63 (1 H, m), 7.60 (1 H, s), 7.52 (2 H, dd, J = 5.9, 3.0), 7.24 (2 H, t, J = 8.2). δ_C (101 MHz, DMSO-d_6) 179.0, 155.5, 141.6, 136.2, 130.7, 129.7, 126.8, 126.3, 125.5, 124.8, 123.1, 123.1, 118.3, 113.5, 112.8, 110.6, 108.5, 82.9.

5-Nitro-1,2,3,4-tetrahydrochromeno[3′,2′:5,6]pyrido[1,2-a]pyrimidin-7(12aH)-one (7b). Yellow solid; yield: 84% (0.251 g); mp 226−228 °C; δ_H (400 MHz, DMSO-d_6) 10.65 (1 H, s), 7.92 (1 H, d, J = 5.0), 7.85−7.75 (1 H, m), 7.60 (1 H, dd, J = 11.1, 4.2), 7.16 (1 H, t, J = 7.5), 7.08 (1 H, d, J = 8.2), 6.33 (1 H, s), 3.93−3.78 (1 H, m), 3.61 (2 H, t, J = 14.8), 3.46 (1 H, s), 2.09 (1 H, dd, J = 8.7, 4.6), 2.03−1.88 (1 H, m). δ_C (101 MHz, DMSO-d_6) 179.6, 156.2, 150.0, 136.0, 127.0, 126.8, 123.0, 122.6, 118.1, 111.6, 109.8, 87.3, 45.0, 38.7, 18.3.

8-Methyl-4-nitro-2,3-dihydro-1H-chromeno[3,2-e]-imidazo[1,2-a]pyridin-6(11aH)-one (7c). Yellow solid; yield: 85% (0.254 g); mp 232−234 °C; δ_H (400 MHz, DMSO-d_6) 9.56 (1 H, s), 7.80 (1 H, s), 7.58 (1 H, d, J = 1.2), 7.39 (1 H, dd, J = 8.4, 1.8), 6.96 (1 H, d, J = 8.3), 6.29 (1 H, s), 4.11 (1 H, td, J = 9.3, 5.6), 3.96−3.82 (2 H, m), 3.81−3.65 (1 H, m), 2.28 (3 H, s). δ_C (101 MHz, DMSO-d_6) 179.0, 154.0, 153.7, 136.6, 131.7, 127.2, 126.4, 122.6, 117.8, 112.0, 108.3, 84.8, 46.2, 43.3, 20.0. HRMS (ESI) m/z: [M + H]$^+$ calcd for $C_{15}H_{13}N_3NaO_4^+$ 322.0804, found 322.0810.

4-Nitro-2,3-dihydro-1H-chromeno[3,2-e]imidazo[1,2-a]-pyridin-6(11aH)-one (7d). Yellow solid; yield: 86% (0.245 g); mp 238−240 °C; δ_H (400 MHz, DMSO-d_6) 9.57 (1 H, s), 7.86−7.76 (1 H, m), 7.60 (1 H, t, J = 7.1), 7.16 (1 H, t, J = 7.1), 7.07 (1 H, d, J = 8.0), 6.35 (1 H, s), 4.14 (1 H, dd, J = 4.4),

3.98−3.75 (1 H, m). δ_C (101 MHz, DMSO-d_6) 179.5, 156.4, 154.0, 136.4, 127.7, 127.1, 123.2, 123.0, 118.4, 112.2, 108.7, 85.2, 46.5, 43.6.

8-Fluoro-4-nitro-2,3-dihydro-1H-chromeno[3,2-e]-imidazo[1,2-a]pyridin-6(11aH)-one (7e). Yellow solid; yield: 83% (0.251 g); mp 230−232 °C; δ_H (400 MHz, DMSO-d_6) 9.62 (1 H, s), 7.85 (1 H, s), 7.47 (2 H, dd, J = 13.5, 5.6), 7.13 (1 H, dd, J = 8.1, 4.2), 6.36 (1 H, s), 4.13 (1 H, td, J = 9.2, 5.5), 3.97−3.73 (3 H, m). δ_C (101 MHz, DMSO-d_6) 178.2, 156.0, 156.0, 153.6, 152.4, 152.3, 128.0, 123.9, 123.8, 120.3, 120.2, 111.9, 111.6, 111.0, 110.9, 108.5, 85.1, 46.2, 43.3. HRMS (ESI) m/z: [M + H]$^+$ calcd for $C_{14}H_{11}FN_3O_4^+$ 304.0734, found 304.0733.

General Procedure for the Synthesis of Indolybenzo-furanoimidazopyridine Derivatives (8a−c). A 10 mL round-bottomed flask was charged with synthesized indolyli-midazopyridines **1** (1.0 mmol) and phenacyl bromide **2** (1.5 mmol) in DMF (3 mL), and K_2CO_3 (3 mmol) was added to the reaction mixture and heated in an oil bath at 120 °C for the stipulated period. The consumption of the starting material was monitored by TLC using a simple workup. The precipitated solid was filtered and washed with ethanol (2 to 3 mL) and dried under a vacuum to obtain the pure products in excellent yields (90−95%) without any further purification. The identities of all the synthesized products were confirmed by NMR and ESI-MS, which were in good agreement with those of the assigned structures.

(3-(5-(1H-Indol-3-yl)-8-nitro-1,2,3,5-tetrahydroimidazo-[1,2-a]pyridin-6-yl)benzofuran-2-yl)(phenyl)methanone (8a). Pale red solid; yield: 95% (0.477 g); mp 290−292 °C; ^{1}H NMR (400 MHz, DMSO-d_6) δ 10.98 (s, 1H), 9.13 (s, 1H), 7.77 (s, 4H), 7.68 (dd, J = 10.7, 7.0 Hz, 2H), 7.55 (d, J = 8.0 Hz, 1H), 7.46 (d, J = 7.4 Hz, 2H), 7.35 (s, 1H), 7.30−7.20 (m, 2H), 7.11 (s, 1H), 7.02−6.96 (m, 1H), 6.94−6.87 (m, 1H), 6.05 (s, 1H), 3.73−3.56 (m, 3H), 3.08 (d, J = 8.6 Hz, 1H). ;^{13}C NMR (101 MHz, DMSO-d_6) δ 184.1, 155.0, 154.2, 146.9, 136.9, 136.6, 132.2, 132.0, 131.7, 129.2, 127.9, 127.8, 127.5, 125.7, 125.5, 124.5, 122.5, 121.9, 119.7, 118.6, 114.4, 112.8, 112.3, 111.5, 107.4, 54.9, 47.2, 42.8. ESI-MS m/z: [M + H]$^+$ calcd for $C_{30}H_{23}N_4O_4^+$ 503.5380, found 503.9274.

(3-(5-(1H-Indol-3-yl)-8-nitro-1,2,3,5-tetrahydroimidazo-[1,2-a]pyridin-6-yl)benzofuran-2-yl)(4-chlorophenyl)-methanone (8b). Dark brown solid; yield: 94% (0.505 g); mp 278−280 °C; ^{1}H NMR (400 MHz, DMSO-d_6) δ 10.97 (s, 1H), 9.13 (s, 1H), 7.85 (d, J = 8.0 Hz, 2H), 7.65 (dd, J = 14.0, 8.1 Hz, 3H), 7.55 (d, J = 8.3 Hz, 1H), 7.45 (t, J = 7.5 Hz, 2H), 7.35 (s, 1H), 7.28 (t, J = 7.6 Hz, 1H), 7.23 (d, J = 8.0 Hz, 1H), 7.14−7.07 (m, 1H), 6.99 (t, J = 7.5 Hz, 1H), 6.91 (t, J = 7.6 Hz, 1H), 6.06 (s, 1H), 3.78−3.54 (m, 3H), 3.15−3.01 (m, 1H). ^{13}C NMR (101 MHz, DMSO-d_6) δ 183.9, 155.6, 155.0, 154.2, 146.9, 138.3, 136.9, 136.3, 131.6, 129.2, 129.1, 127.9, 127.8, 125.7, 125.5, 124.5, 122.5, 121.9, 119.7, 118.6, 114.4, 112.8, 112.3, 111.5, 107.3, 54.9, 47.2, 42.8. HRMS (ESI) m/z: [M + H]$^+$ calcd for $C_{30}H_{22}ClN_4O_4^+$ 537.1330, found 537.1318.

(3-(5-(1H-Indol-3-yl)-8-nitro-1,2,3,5-tetrahydroimidazo-[1,2-a]pyridin-6-yl)benzofuran-2-yl)(4-bromophenyl)-methanone (8c). Pale red solid; yield: 93% (0.541 g); mp 265−267 °C; ^{1}H NMR (400 MHz, DMSO-d_6) δ 10.95 (s, 1H), 9.10 (s, 1H), 7.77 (s, 4H), 7.67 (dd, J = 13.8, 6.2 Hz, 2H), 7.55 (d, J = 8.3 Hz, 1H), 7.45 (d, J = 7.8 Hz, 2H), 7.34 (d, J = 1.0 Hz, 1H), 7.28 (t, J = 7.5 Hz, 1H), 7.23 (d, J = 8.1 Hz, 1H), 7.10 (d, J = 2.1 Hz, 1H), 6.99 (t, J = 7.5 Hz, 1H), 6.93−6.88 (m, 1H), 6.04 (s, 1H), 3.68−3.55 (m, 3H), 3.09 (d,

J = 8.9 Hz, 1H). ^{13}C NMR (101 MHz, DMSO-d_6) δ 183.7, 155.0, 154.4, 149.9, 146.6, 142.9, 136.9, 130.9, 129.6, 128.8, 127.8, 125.8, 125.5, 124.6, 124.0, 123.0, 122.7, 121.9, 119.7, 118.6, 114.0, 112.9, 112.4, 111.5, 107.4, 54.9, 47.2, 42.8. HRMS (ESI) *m/z*: [M + H]$^+$ calcd for $C_{30}H_{22}BrN_4O_4^+$ 581.0824, found 581.0804.

ASSOCIATED CONTENT

Supporting Information

The Supporting Information is available free of charge at https://pubs.acs.org/doi/10.1021/acsomega.2c04990.

^{1}H NMR and ^{13}C{^{1}H} NMR spectral data for all synthesized compounds; HRMS (ESI) spectral data for **6a−b**, **6d−f**, **6h−o**, **7c**, **7e**, and **8a−c**; ORTEP diagram of compound **6h**; green matrix factors: atom economy and E-factor calculation for representative compounds such as **6a**, **7a** and **8a**; and DFT and docking studies for all the synthesized compounds except **8a−c** (PDF)

AUTHOR INFORMATION

Corresponding Authors

Kamalraja Jayabal − *Department of Chemistry, Pondicherry University, Puducherry 605014, India; Department of Applied Chemistry, National Yang Ming Chiao Tung University, Hsinchu 30010, Taiwan R.O.C;* orcid.org/0000-0003-3312-7588; Email: jkamalraja@yahoo.com

Shih-Ching Chuang − *Department of Applied Chemistry, National Yang Ming Chiao Tung University, Hsinchu 30010, Taiwan R.O.C;* orcid.org/0000-0002-6926-9812; Email: jscchuang@nycu.edu.tw

Authors

Dhanasekar Elumalai − *Department of Chemistry, Pondicherry University, Puducherry 605014, India*

Saraswathi Leelakrishnan − *Department of Chemistry, Pondicherry University, Puducherry 605014, India; Department of Chemistry, Nirmala College for Women, Coimbatore 641018, India*

Suman Bhattacharya − *Department of Physics, University of Limerick, Limerick V94 T9PX, Republic of Ireland;* orcid.org/0000-0001-9767-7779

Venkatesan Rengarajan − *Department of Chemistry, Pondicherry University, Puducherry 605014, India;* orcid.org/0000-0001-9561-1098

Tharanikkarasu Kannan − *Department of Chemistry, Pondicherry University, Puducherry 605014, India;* orcid.org/0000-0003-4426-983X

Complete contact information is available at:
https://pubs.acs.org/10.1021/acsomega.2c04990

Notes

The authors declare no competing financial interest.

ACKNOWLEDGMENTS

REFERENCES

(1) Yin, Y.; Wunderink, R. G. MERS, SARS and other coronaviruses as causes of pneumonia. *Respirology* **2018**, *23*, 130−137.

(2) Zhu, H.; Wei, L.; Niu, P. The novel coronavirus outbreak in Wuhan, China. *Global Health Res. Policy* **2020**, *5*, 1.

(3) (a) Morawska, L.; Cao, J. Airborne transmission of SARS-CoV-2: The world should face the reality. *Environ. Int.* **2020**, *139*, No. 105730. (b) Tang, S.; Mao, Y.; Jones, R. M.; Tan, Q.; Ji, J. S.; Li, N.; Shen, J.; Lv, Y.; Pan, L.; Ding, P.; Wang, X.; Wang, Y.; MacIntyre, C. R.; Shia, X. Aerosol transmission of SARS-CoV-2? Evidence, prevention and control. *Environ. Int.* **2020**, *144*, No. 106039.

(4) (a) Ragia, G.; Manolopoulos, V. G. Inhibition of SARS-CoV-2 entry through the ACE2/TMPRSS2 pathway: a promising approach for uncovering early COVID-19 drug therapies. *Eur. J. Clin. Pharmacol.* **2020**, *76*, 1623−1630. (b) Shulla, A.; Heald-Sargent, T.; Subramanya, G.; Zhao, J.; Perlman, S.; Gallagher, T. A Transmembrane Serine Protease Is Linked to the Severe Acute Respiratory Syndrome Coronavirus Receptor and Activates Virus Entry. *J. Virol.* **2011**, *85*, 873−882.

(5) Callaway, E. Delta coronavirus variant: scientists brace for impact. *Nature* **2021**, *595*, 17−18.

(6) Dejnirattisai, W.; Zhou, D.; Supasa, P.; Liu, C.; Mentzer, A. J.; Ginn, H. M.; Zhao, Y.; Duyvesteyn, H. M. E.; Tuekprakhon, A.; Nutalai, R.; Wang, B.; Lopez-Camacho, C.; Slon-Campos, J.; Walter, T. S.; Skelly, D.; Costa Clemens, S. A.; Naveca, F. G.; Nascimento, V.; Nascimento, F.; Fernandes da Costa, C.; Resende, P. C.; Pauvolid-Correa, A.; Siqueira, M. M.; Dold, C.; Levin, R.; Dong, T.; Pollard, A. J.; Knight, J. C.; Crook, D.; Lambe, T.; Clutterbuck, E.; Bibi, S.; Flaxman, A.; Bittaye, M.; Belij-Rammerstorfer, S.; Gilbert, S. C.; Carroll, M. W.; Klenerman, P.; Barnes, E.; Dunachie, S. J.; Paterson, N. G.; Williams, M. A.; Hall, D. R.; Hulswit, R. J. G.; Bowden, T. A.; Fry, E. E.; Mongkolsapaya, J.; Ren, J.; Stuart, D. I.; Screaton, G. R. Antibody evasion by the P.1 strain of SARS-CoV-2. *Cell* **2021**, *184*, 2939−2954.e9.

(7) Savi, C. D.; Hughes, D. L.; Kvaerno, L. Quest for a COVID-19 Cure by Repurposing Small-Molecule Drugs: Mechanism of Action, Clinical Development, Synthesis at Scale, and Outlook for Supply. *Org. Process Res. Dev.* **2020**, *24*, 940−976.

(8) (a) Vieira, T.; Stevens, A. C.; Chtchemelinine, A.; Gao, D.; Badalov, P.; Heumann, L. Development of a Large-Scale Cyanation Process Using Continuous Flow Chemistry En Route to the Synthesis of Remdesivir. *Org. Process Res. Dev.* **2020**, *24*, 2113−2121. (b) Keutz, T.; Williams, J. D.; Kappe, C. O. Flash Chemistry Approach to Organometallic C-Glycosylation for the Synthesis of Remdesivir. *Org. Process Res. Dev.* **2021**, *25*, 1015−1021. (c) Gannedi, V.; Villuri, B. K.; Reddy, S. N.; Ku, C. C.; Wong, C. H.; Hung, S. C. Practical Remdesivir Synthesis through One-Pot Organocatalyzed Asymmetric (S)-P-Phosphoramidation. *J. Org. Chem.* **2021**, *86*, 4977−4985.

(9) (a) Huang, B.; Zeng, L.; Shen, Y.; Cui, S. One-Pot Multicomponent Synthesis of β-Amino Amides. *Angew. Chem., Int. Ed.* **2017**, *56*, 4565−4568. (b) Sun, S.; Zhou, C.; Yu, J. T.; Cheng, J. Visible-Light-Driven Palladium-Catalyzed Oxy-Alkylation of 2-(1-Arylvinyl)anilines by Unactivated Alkyl Bromides and CO$_2$: Multicomponent Reactions toward 1,4-Dihydro-2H-3,1-benzoxazin-2-ones. *Org. Lett.* **2019**, *21*, 6579−6583. (c) Li, J.; Daniliuc, C. G.; Mück-Lichtenfeld, C.; Kehr, G.; Erker, G. Multi-Component Synthesis of Rare 1,3-Dihydro-1,3-azaborinine Derivatives: Application of a Bora-Nazarov Type Reaction. *Angew. Chem., Int. Ed.* **2019**, *58*, 15377−15380. (d) Huang, H. M.; Bellotti, P.; Pflüger, P. M.; Schwarz, J. L.; Glorius, H. B.; Three-Component, F. Interrupted Radical Heck/Allylic Substitution Cascade Involving Unactivated Alkyl Bromides. *J. Am. Chem. Soc.* **2020**, *142*, 10173. (e) Tan, X.; Hou, X.; Rogge, T.; Ackermann, L. Ruthenaelectro-Catalyzed Domino Three-Component Alkyne Annulation for Expedient Isoquinoline Assembly. *Am. Ethnol.* **2021**, *60*, 4619−4624.

(10) (a) Sravanthi, T. V.; Manju, S. L. Indoles — A promising scaffold for drug development. *Euro. J. Pharm. Sci.* **2016**, *91*, 1−10. (b) Chadha, N.; Silakari, O. Indoles as therapeutics of interest in medicinal chemistry: Bird's eye view. *Eur. J. Med. Chem.* **2017**, *134*, 159−184. (c) Kumari, A.; Singh, R. K. Medicinal chemistry of indole derivatives: Current to future therapeutic prospectives. *Bioorganic Chemistry.* **2019**, *89*, No. 103021.

(11) Dai, W.; Zhang, B.; Jiang, X.; Su, H.; Li, J.; Zhao, Y.; Xie, X.; Jin, Z.; Peng, J.; Liu, F.; Li, C.; Li, Y.; Bai, F.; Wang, H.; Cheng, X.; Cen, X.; Hu, S.; Yang, X.; Wang, J.; Liu, X.; Xiao, G.; Jiang, H.; Rao, Z.; Zhang, L.; Xu, Y.; Yang, H.; Liu, H. Structure-based design of antiviral drug candidates targeting the SARS-CoV-2 main protease. *Science* **2020**, *368*, 1331−1335.

(12) Hattori, S.; Kuwata, N. H.; Hayashi, H.; Allu, S. R.; Raghavaiah, J.; Bulut, H.; Das, D.; Anson, B. J.; Lendy, E. K.; Takamatsu, Y.; Takamune, N.; Kishimoto, N.; Murayama, K.; Hasegawa, K.; Li, M.; Davis, D. A.; Kodama, E. N.; Yarchoan, R.; Wlodawer, A.; Misumi, S.; Mesecar, A. D.; Ghosh, A. K.; Mitsuya, H. A small molecule compound with an indole moiety inhibits the main protease of SARS-CoV-2 and blocks virus replication. *Nat. Commun.* **2021**, *12*, 668.

(13) Ghosh, A. K.; Raghavaiah, J.; Shahabi, D.; Yadav, M. B.; Anson, J.; Lendy, E. K.; Hattori, S. I.; Higashi-Kuwata, N.; Mitsuya, H.; Mesecar, A. D. Indole Chloropyridinyl Ester-Derived SARS-CoV-2 3CLpro Inhibitors: Enzyme Inhibition, Antiviral Efficacy, Structure−Activity Relationship, and X-ray Structural Studies. *J. Med. Chem.* **2021**, *64*, 14702−14714.

(14) Boras, B.; Jones, R. M.; Anson, B. J.; Arenson, D.; Aschenbrenner, L.; Bakowski, M. A.; Beutler, N.; Binder, J.; Chen, E.; Eng, H.; Hammond, H.; Hammond, J.; Haupt, R. E.; Hoffman, R.; Kadar, E. P.; Kania, R.; Kimoto, E.; Kirkpatrick, M. G.; Lanyon, L.; Lendy, E. K.; Lillis, J. R.; Logue, J.; Luthra, S. A.; Ma, C.; Mason, S. W.; McGrath, M. E.; Noell, S.; Obach, R. S.; O'Brien, M. N.; O'Connor, R.; O'gilvie, K.; Owen, D.; Pettersson, M.; Reese, M. R.; Rogers, T. F.; Rossulek, M. I.; Sathish, J. G.; Shirai, N.; Steppan, C.; Ticehurst, M.; Updyke, L. W.; Weston, S.; Zhu, Y.; Wang, J.; Chatterjee, A. K.; Mesecar, A. D.; Frieman, M. B.; Anderson, A. S.; Allerton, C. Discovery of a Novel Inhibitor of Coronavirus 3CL Protease for the Potential Treatment of COVID-19. *BioRxiv* **2021**, 2020.

(15) Vijayakumar, B. G.; Ramesh, D.; Joji, A.; Jayadharini, J. P.; Kannan, T. In silico pharmacokinetic and molecular docking studies of natural flavonoids and synthetic indole chalcones against essential proteins of SARS-CoV-2. *Eur. J. Pharmacol.* **2020**, *886*, No. 173448.

(16) (a) Hosseini, H.; Bayat, M. An efficient synthesis of new imidazo[1,2-*a*]pyridine-6-carbohydrazide and pyrido[1,2-*a*]-pyrimidine-7-carbohydrazide derivatives *via* a five-component cascade reaction. *RSC Adv.* **2019**, *9*, 7218−7227. (b) Vanda, D.; Zajdel, P.; Soural, M. Imidazopyridine-based selective and multifunctional ligands of biological targets associated with psychiatric and neuro-degenerative diseases. *Eur. J. Med. Chem.* **2019**, *181*, No. 111569. (c) Rosse, G. Pyridopyrimidines as Inhibitors of Hepatitis C Virus. *ACS Med. Chem. Lett.* **2014**, *5*, 226−227. (d) Krapf, M. K.; Gallus, J.; Vahdati, S.; Wiese, M. New Inhibitors of Breast Cancer Resistance Protein (ABCG2) Containing a 2,4-Disubstituted Pyridopyrimidine Scaffold. *J. Med. Chem.* **2018**, *61*, 3389−3408. (e) Nasri, S.; Bayat, M.; Farahani, H. V.; Karami, S. Synthesis of new functionalized thiazolo pyridine-fused and thiazolo pyridopyrimidine-fused spirooxindoles *via* one-pot reactions. *Heliyon.* **2020**, *6*, No. e03687.

(17) (a) Babu, T. H.; Kamalraja, J.; Muralidharan, D.; Perumal, P. T. Michael addition of α-azido ketones on iminocoumarin derivatives: An efficient access to new functionalized azido chromenes. *Tetrahedron Lett.* **2011**, *52*, 4093−4096. (b) Kamalraja, J.; Babu, T. H.; Muralidharan, D.; Perumal, P. T. A Facile Method for the Synthesis of 3-(Aminomethylene)oxindoles from Isatylidene Malononitriles and α-Azido Ketones. *Synlett* **2012**, *23*, 1950−1954. (c) Kamalraja, J.; Sowndarya, R.; Perumal, P. A Greener Approach for the Regioselective Synthesis of Multifunctionalized Indolylpyrrole and Indolyltriazolylpyrrole Hybrids via Michael Addition of α-Azido Ketones. *Synlett* **2014**, *25*, 2208−2212. (d) Kamalraja, J.; Murugasan,

P.; Perumal, P. T. InCl$_3$-mediated eco-friendly three-component domino reaction for synthesis of highly functionalized triazolylspir-oxindolinopyrans and triazolylpyrans under solvent-free conditions. *RSC Adv.* **2014**, *4*, 19422−19432. (e) Dhanasekar, E.; Kannan, T.; Venkatesan, R.; Perumal, P. T.; Kamalraja, J. Metal-Free and Regioselective Synthesis of Substituted and Fused Chromenopyrrole Scaffolds *via* the Divergent Reactivity of α-Azido Ketones in Water. *J. Org. Chem.* **2020**, *85*, 9631−9649.

(18) (a) Kamalraja, J.; Muralidharan, D.; Perumal, P. An Efficient, One-Pot Regioselective Synthesis of Highly Functionalized Chromen-5-ones and Pyrano[3,2-*c*]chromen-5-ones via a Tandem Knoevena-gel−Michael−Cyclization Sequence. *Synlett* **2012**, *23*, 2894−2898. (b) Poomathi, N.; Kamalraja, J.; Mayakrishnan, S.; Muralidharan, D.; Perumal, P. Indium Trichloride Catalysed Domino Reactions of Isatin: A Facile Access to the Synthesis of Spiro(indoline-3,4′-pyrano[2,3-*c*]pyrazol)-2-one Derivatives. *Synlett* **2014**, *25*, 708−712. (c) Kamalraja, J.; Perumal, P. T. Microwave assisted InCl$_3$ mediated regioselective synthesis of highly functionalized indolylpyran under solvent-free condition and its chemical transformation to indolyl-triazolylpyran hybrids. *Tetrahedron Lett.* **2014**, *55*, 3561−3564. (d) Jayabal, K.; Paramasivan, T. P. An expedient four-component domino protocol for the regioselective synthesis of highly function-alized pyranopyrazoles and chromenopyrazoles via nitroketene-*N,S*-acetal chemistry under solvent-free condition. *Tetrahedron Lett.* **2014**, *55*, 2010−2014. (e) Kandhasamy, S.; Ramanathan, G.; Kamalraja, J.; Balaji, R.; Mathivanan, N.; Sivagnanam, U. T.; Perumal, P. T. Synthesis, characterization and biological evaluation of chromen and pyrano chromen-5-one derivatives impregnated into a novel collagen based scaffold for tissue engineering applications. *RSC Adv.* **2015**, *5*, 55075−55087. (f) Elumalai, D.; Gnanasekaran, R.; Leelakrishnan, S.; Nachimuthu, G.; Kannan, T.; Paramasivam, T. P.; Jayabal, K. InCl$_3$-Assisted Eco-Friendly Approach for N-Fused 1,4-Dihydropyridine Scaffolds via Ring Opening Michael Addition of Cyclic Nitroketene and Iminocoumarin: Synthesis and DFT Studies. *ChemistrySelect* **2018**, *3*, 2070−2079. (g) Maganti, L. H. B.; Ramesh, D.; Vijayakumar, B. G.; Khan, M. I. K.; Dhayalan, A.; Kamalraja, J.; Kannan, T. Acetylene containing 2-(2-hydrazinyl)thiazole derivatives: design, synthesis, and *in vitro* and *in silico* evaluation of antimycobacterial activity against *Mycobacterium tuberculosis*. *RSC Adv.* **2022**, *12*, 8771−8782.

(19) (a) Kolokythas, G.; Kostakis, I. K.; Pouli, N.; Marakos, P.; Kletsas, D.; Pratsinis, H. Synthesis and cytotoxic activity of some new azapyranoxanthenone aminoderivatives. *Bioorg. Med. Chem.* **2003**, *11*, 4591−4598. (b) Villani, F. J.; Mann, T. A.; Wefer, E. A.; Hannon, J.; Larca, L. L.; Landon, M. J.; Spivak, W.; Vashi, D.; Tozzi, S.; Danko, G.; del Prado, M.; Lutz, R. Benzopyranopyridine derivatives. 1. Aminoalkyl derivatives of the azaxanthenes as bronchodilating agents. *J. Med. Chem.* **1975**, *18*, 1−18.

(20) Meng, W.; Dong, Y.; Liu, J.; Wang, Z.; Zhong, X.; Chen, R.; Zhou, H.; Lin, M.; Jiang, L.; Gao, F.; Xu, T.; Chen, Q.; Zeng, X. A clinical evaluation of amlexanox oral adhesive pellicles in the treatment of recurrent aphthous stomatitis and comparison with amlexanox oral tablets: a randomized, placebo controlled, blinded, multicenter clinical trial. *Trials* **2009**, *10*, 30.

(21) (a) Jamshaid, S.; Mohandoss, S.; Lee, Y. R. Indium(iii)-catalyzed solvent-free multicomponent [2 + 2 + 1 + 1]-annulation to polycyclic functionalized fused pyridines as potential optical chemo-sensors. *Green Chem.* **2021**, *23*, 5113−5119. (b) Sultana, S.; González-Montiel, G. A.; Pradhan, S.; Khanal, H. D.; Nale, S. D.; Cheong, P. H.; Lee, Y. R. In(III)-Catalyzed Direct Regioselective Syntheses of 1-Naphthaldehyde Derivatives *via* a Hidden Aldehyde 1,3-Translocation and Disjointed CO$_2$ Extrusion. *ACS Catal.* **2021**, *11*, 6467−6473. (c) Poomathi, N.; Perumal, P. T.; Ramakrishna, S. An efficient and eco-friendly synthesis of 2-pyridones and function-alized azaxanthone frameworks via indium triflate catalyzed domino reaction. *Green Chem.* **2017**, *19*, 2524−2529. (d) Dipak, P.; Laskar, D. D.; Sandhu, J. S. Indium trifluoromethanesulfonate (In(OTf)$_3$). A novel reusable catalyst for intramolecular Diels−Alder reactions. *Tetrahedron Lett.* **2000**, *41*, 8639−8643. (e) Rawat, D.; Ravi, C.;

Joshie, A.; Suresh, E.; Jana, K.; Ganguly, B.; Adimurthy, S. Indium-Catalyzed Denitrogenative Transannulation of Pyridotriazoles: Synthesis of Pyrido[1,2-*a*]indoles. *Org. Lett.* **2019**, *21*, 2043−2047. (f) Mohammad, A.; Sonaimuthu, M.; Palanisamy, S.; SangGuan, Y.; Won-Guen, Y.; Sung, H. K.; Yong, R. L, Indium-Catalyzed Aromative Spiro Coupling of Quinones with Oxindoles for Highly Functionalized Xanthenes as Efficient Fluorophores. *Org. Lett.* **2021**, *23*, 1383−1387.

(22) *Gaussian 09*, Revision A.02, Frisch, M. J.; Trucks, G. W.; Schlegel, H. B.; Scuseria, G. E.; Robb, M. A.; Cheeseman, J. R.; Scalmani, G.; Barone, V.; Mennucci, B.; Petersson, G. A.; Nakatsuji, H.; Caricato, M.; Li, X.; Hratchian, H. P.; Izmaylov, A. F.; Bloino, J.; Zheng, G.; Sonnenberg, J. L.; Hada, M.; Ehara, M.; Toyota, K.; Fukuda, R.; Hasegawa, J.; Ishida, M.; Nakajima, T.; Honda, Y.; Kitao, O.; Nakai, H.; Vreven, T.; Montgomery, J. A.; Peralta, J. E.; Ogliaro, F.; Bearpark, M.; Heyd, J. J.; Brothers, E.; Kudin, K. N.; Staroverov, V. N.; Kobayashi, R.; Normand, J.; Raghavachari, K.; Rendell, A.; Burant, J. C.; Iyengar, S. S.; Tomasi, J.; Cossi, M.; Rega, N.; Millam, J. M.; Klene, M.; Knox, J. E.; Cross, J. B.; Bakken, V.; Adamo, C.; Jaramillo, J.; Gomperts, R.; Stratmann, R. E.; Yazyev, O.; Austin, A. J.; Cammi, R.; Pomelli, C.; Ochterski, J. W.; Martin, R. L.; Morokuma, K.; Zakrzewski, V. G.; Voth, G. A.; Salvador, P.; Dannenberg, J. J.; Dapprich, S.; Daniels, A. D.; Farkas, O.; Foresman, J. B.; Ortiz, J. V.; Cioslowski, J.; Fox, D. J. Gaussian, Inc., Wallingford CT, 2009.

(23) Han, D. P.; Penn-Nicholson, A.; Cho, M. W. Identification of critical determinants on ACE2 for SARS-CoV entry and development of a potent entry inhibitor. *Virology* **2006**, *350*, 15−25.

(24) (a) Li, W.; Moore, M. J.; Vasilieva, N.; Sui, J.; Wong, S. K.; Berne, M. A.; Somasundaran, M.; Sullivan, J. L.; Luzuriaga, K.; Greenough, T. C.; Choe, H.; Farzan, M. Angiotensin-converting enzyme 2 is a functional receptor for the SARS coronavirus. *Nature* **2003**, *426*, 450−454. (b) Zhao, J.; Li, K.; Wohlford-Lenane, C.; Agnihothram, S. S.; Fett, C.; Zhao, J.; Gale, M. J., Jr.; Baric, R. S.; Enjuanese, L.; Gallagher, T.; McCray, P. B., Jr.; Perlman, S. Rapid generation of a mouse model for Middle Eastrespiratory syndrome. *Proc. Natl. Acad. Sci.* **2014**, *111*, 4970−4975.

(25) Li, F.; Li, W.; Farzan, M.; Harrison, S. C. Structure of SARS coronavirus spike receptor-binding domain complexed with receptor. *Science* **2005**, *309*, 1864−1868.

(26) (a) Harcourt, B. H.; Jukneliene, D.; Kanjanahaluethai, A.; Bechill, J.; Serverson, K. M.; Smith, C. M.; Rota, P. A.; Baker, S. C. Identification of severe acute respiratory syndrome coronavirus replicase products and characterization of papain-like protease activity. *J. Virol.* **2004**, *78*, 13600−13612. (b) Chen, X.; Yang, X.; Zheng, Y.; Yang, Y.; Xing, Y.; Chen, Z. SARS coronavirus papain-like protease inhibits the type I interferon signaling pathway through interaction with the STING-TRAF3-TBK1 complex. *Protein Cell.* **2014**, *5*, 369−381. (c) Yuan, L.; Chen, Z.; Song, S.; Wang, S.; Tian, C.; Xing, G.; Chen, X.; Xiao, Z. X.; He, F.; Zhang, L. p53 degradation by a coronavirus papain-like protease suppresses type I interferon signalling. *J. Biol. Chem.* **2015**, *290*, 3172−3182.

(27) (a) Wan, Y.; Shang, J.; Graham, R.; Baric, R. S.; Li, F. Receptor Recognition by the Novel Coronavirus from Wuhan: an Analysis Based on Decade-Long Structural Studies of SARS Coronavirus. *J. Virol.* **2020**, *94*, No. e00127-20. (b) Xu, X.; Chen, P.; Wang, J.; Feng, J.; Zhou, H.; Li, X.; Zhong, W.; Hao, P. Evolution of the novel coronavirus from the ongoing Wuhan outbreak and modeling of its spike protein for risk of human transmission. *Sci China Life Sci.* **2020**, *63*, 457−460.

(28) Yang, H.; Xie, W.; Xue, X.; Yang, K.; Ma, J.; Liang, W.; Zhao, Q.; Zhou, Z.; Pei, D.; Ziebuhr, J.; Hilgenfeld, R.; Yuen, K. W.; Wong, L.; Gao, G.; Chen, S.; Zhu, C.; Ma, D.; Bartlam, M.; Rao, Z. Design of Wide-Spectrum Inhibitors Targeting Coronavirus Main Proteases. *PLoS Biol.* **2005**, *3*, 1742−1752.

(29) (a) Pillaiyar, T.; Maickam, M.; Namasivayam, V.; Hayashi, Y.; Jung, S. H. An Overview of Severe Acute Respiratory Syndrome-Coronavirus (SARS-CoV) 3CL Protease Inhibitors: Peptidomimetics and Small Molecule Chemotherapy. *J. Med. Chem.* **2016**, *59*, 6595−6628. (b) Dai, W.; Jochmans, D.; Xie, H.; Yang, H.; Li, J.; Su, H.;

Chang, D.; Wang, J.; Peng, J.; Zhu, L.; Nian, Y.; Hilgenfeld, R.; Jiang, H.; Chen, K.; Zhang, L.; Xu, Y.; Neyts, J.; Liu, H. Design, Synthesis, and Biological Evaluation of Peptidomimetic Aldehydes as Broad-Spectrum Inhibitors against Enterovirus and SARS-CoV-2. *J. Med. Chem.* **2021**, *65*, 2794−2808.

(30) Millet, J. K.; Whittaker, G. R. Host cell proteases: Critical determinants of coronavirus tropism and pathogenesis. *Virus Res.* **2015**, *202*, 120−134.

(31) Xia, S.; Liu, Q.; Wang, Q.; Sun, Z.; Su, S.; Du, L. Middle East respiratory syndrome coronavirus (MERS-CoV) entry inhibitors targeting spike protein. *Virus Res.* **2014**, *194*, 200−210.

(32) (a) Shang, J.; Wan, Y.; Luo, C.; Ye, G.; Geng, Q.; Auerbach, A.; Li, F. Cell entry mechanisms of SARS-CoV-2. *Proc. Natl. Acad. Sci.* **2020**, *117*, 11727−11734. (b) Lan, J.; Ge, J.; Yu, J.; Shan, S.; Zhou, H.; Fan, S.; Zhang, Q.; Shi, X.; Wang, Q.; Zhang, L.; Wang, X. Structure of the SARS-CoV-2 spike receptor-binding domain bound to the ACE2 receptor. *Nature* **2020**, *581*, 215−220.

(33) Nakagawa, K.; Lokugamage, K. G.; Makino, S. Five - Viral and Cellular mRNA Translation in Coronavirus-Infected Cells. *Adv. Virus Res.* **2016**, *96*, 165−192.

(34) Wrapp, D.; Wang, N.; Corbett, K. S.; Goldsmith, J. A.; Hsieh, C. L.; Abiona, O.; Graham, B. S.; McLellan, J. S. Cryo-EM structure of the 2019-nCoV spike in the prefusion conformation. *Science* **2020**, *367*, 1260−1263.

(35) Yan, R.; Zhang, Y.; Li, Y.; Xia, L.; Guo, Y.; Zhou, Q. Structural basis for the recognition of SARS-CoV-2 by full-length human ACE2. *Science* **2020**, *367*, 1444−1448.

(36) Tse, L. V.; Hamilton, A. M.; Friling, T.; Whittaker, G. R. A Novel Activation Mechanism of Avian Influenza Virus H9N2 by Furin. *J. Virol.* **2014**, *88*, 1673−1683.

(37) Cantuti-Castelvetri, L.; Ojha, R.; Pedro, L. D.; Djannatian, M.; Franz, J.; Kuivanen, S.; Van der Meer, F.; Kallio, K.; Kaya, T.; Anastasina, M.; Smura, T.; Levanov, L.; Szirovicza, L.; Tobi, A.; Kallio-Kokko, H.; Österlund, P.; Joensuu, M.; Meunier, F. A.; Butcher, S. J.; Sebastian Winkler, M.; Mollenhauer, B.; Helenius, A.; Gokce, O.; Teesalu, T.; Hepojoki, J.; Vapalahti, O.; Stadelmann, C.; Balistreri, G.; Simons, M. Neuropilin-1 facilitates SARS-CoV-2 cell entry and infectivity. *Science* **2020**, *370*, 856−860.

(38) Hoffman, M.; Kleine-Weber, H.; Schroeder, S.; Krüger, N.; Herrler, T.; Erichsen, S.; Schiergens, T. S.; Herrler, G.; Wu, N.-H.; Nitsche, A.; Müller, M. A.; Drosten, C.; Pöhlmann, S. SARS-CoV-2 Cell Entry Depends on ACE2 and TMPRSS2 and Is Blocked by a Clinically Proven Protease Inhibitor. *Cell* **2020**, *181*, 271−280.e8.

(39) Cai, Y.; Zhang, J.; Xiao, T.; Peng, H.; Sterling, S. M.; Walsh, R. M., Jr.; Rawson, S.; Rits-Volloch, S.; Chen, B. Distinct conformational states of SARS-CoV-2 spike protein. *Science* **2020**, *369*, 1586−1592.

(40) https://www.rcsb.structure/6LU7.

(41) Trott, O.; Olson, A. J. AutoDock Vina, AutoDock Vina: improving the speed and accuracy of docking with a new scoring function, efficient optimization and multithreading. *J. Comput. Chem.* **2010**, *31*, 455−461.

(42) https://www.rcsb.structure/7NX7.

(43) https://www.molinspiration.com/cgi-bin/properties.

(44) https://www.preadmet.bmdrc.kr.